HHS Public Access

Author manuscript

Cell. Author manuscript; available in PMC 2022 December 22.

Published in final edited form as:

Cell. 2021 December 22; 184(26): 6344–6360.e18. doi:10.1016/j.cell.2021.11.019.

A genetically defined insula-brainstem circuit selectively controls motivational vigor

Hanfei Deng[1,6,*], **Xiong Xiao**[1,4,6], **Tao Yang**[1], **Kimberly Ritola**[2], **Adam Hantman**[2], **Yulong Li**[3], **Z. Josh Huang**[1,5], **Bo Li**[1,7,*]

[1]Cold Spring Harbor Laboratory, Cold Spring Harbor, NY 11724, USA

[2]HHMI Janelia Research Campus, Ashburn, VA 20147, USA

[3]State Key Laboratory of Membrane Biology, Peking University School of Life Sciences, Beijing 100871, China

[4]Current address: Institute of Neuroscience, CAS Center for Excellence in Brain Science and Intelligence Technology, Chinese Academy of Sciences, Shanghai 200031, China

[5]Current address: Department of Neurobiology, Duke University School of Medicine, Durham, NC 27710, USA

[6]These authors contributed equally

[7]Lead Contact

SUMMARY

The anterior insular cortex (aIC) plays a critical role in cognitive and motivational control of behavior, but the underlying neural mechanism remains elusive. Here we show that aIC neurons expressing *Fezf2* (aIC^{Fezf2}), which are the pyramidal tract neurons, signal motivational vigor and invigorate need-seeking behavior through projections to the brainstem nucleus tractus solitarii (NTS). aIC^{Fezf2} neurons and their postsynaptic NTS neurons acquire anticipatory activity through learning, which encodes the perceived value and the vigor of actions to pursue homeostatic needs. Correspondingly, aIC→NTS circuit activity controls vigor, effort and striatal dopamine release, but only if the action is learned and the outcome is needed. Notably, aIC^{Fezf2} neurons do not represent taste or valence. Moreover, aIC→NTS activity neither drives reinforcement nor influences total consumption. These results pinpoint specific functions of aIC→NTS circuit for

[*]Correspondence: deng@cshl.edu (H.D.); bli@cshl.edu (B.L.).

AUTHOR CONTRIBUTIONS

H.D., X.X. and B.L. designed the study. H.D. and X.X. conducted experiments and analyzed data. T.Y. implemented the *in vivo* imaging methods. K.R. and A.H. generated the rabies viral tracing system. Y.L. developed the dopamine sensor. Z.J.H. generated the *Fezf2-CreER* mouse driver and provided critical reagents and advice. H.D., X.X. and B.L. wrote the paper with inputs from all authors.

DECLARATION OF INTERESTS

The authors declare no competing interests.

selectively controlling motivational vigor, and suggest that motivation is subserved, in part, by aIC's top-down regulation of dopamine signaling.

Graphical Abstract

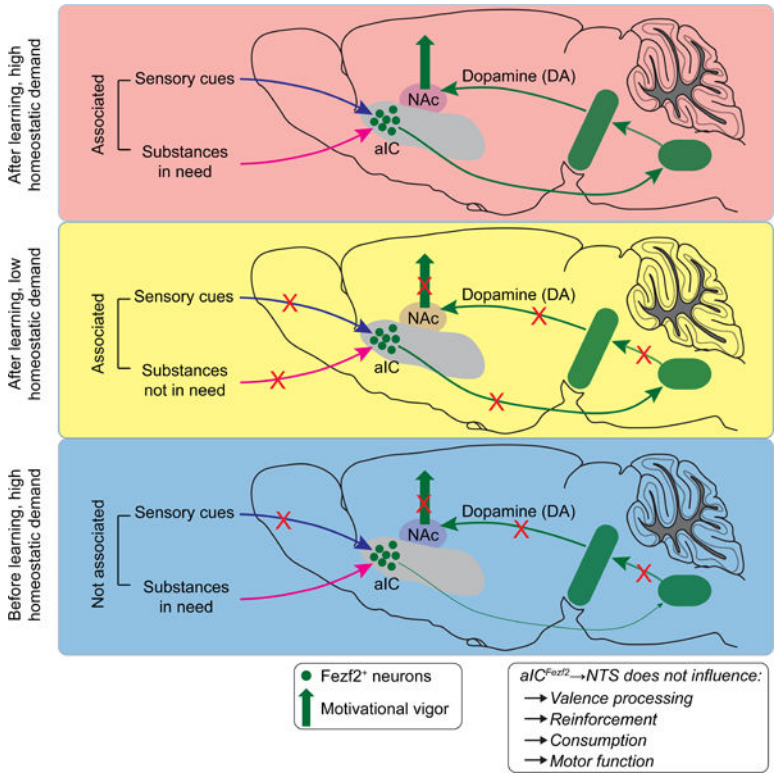

In Brief

An anterior insula-brainstem circuit is defined that specifically controls motivational vigor and dopamine release in a learning- and need-dependent manner, without influencing valence processing, reinforcement, consumption, and motor function.

INTRODUCTION

An extensive body of literature from human studies indicates that the insular cortex (IC), especially the anterior IC (aIC), plays a pivotal role in integrating interoceptive and exteroceptive information into cognitive and motivational control of behavior (Craig, 2009; Critchley and Harrison, 2013; Menon and Uddin, 2010; Quadt et al., 2018). In particular, human neuroimaging studies show that the aIC is more activated during intrinsically motivating tasks than non-motivating ones (Lee and Reeve, 2013, 2017). Cues associated with drugs of abuse activate the IC in addicted individuals, with the activity positively correlated with self-reported craving (Bonson et al., 2002; Engelmann et al., 2012; Kuhn and Gallinat, 2011; Luijten et al., 2011). In parallel, it has been reported that individuals with insular lesions have reduced energy or drive (Manes et al., 1999), or quit smoking easily without relapse (Naqvi et al., 2014; Naqvi et al., 2007). Furthermore, aIC dysfunction is

associated with mood disorders including depression (Etkin, 2010; Mutschler et al., 2019; Paulus and Stein, 2010; Sliz and Hayley, 2012; Sprengelmeyer et al., 2011; Stratmann et al., 2014). These studies strongly suggest a role of the aIC in motivation-related processes.

Studies in rodents have enabled to reveal detailed, yet divergent functions of the IC (Gogolla, 2017; Vincis and Fontanini, 2016). For example, IC neurons are involved in processing gustatory information (Chen et al., 2020; Chen et al., 2011; Katz et al., 2001; Samuelsen and Fontanini, 2017) and cue-reward association (Kusumoto-Yoshida et al., 2015; Livneh et al., 2017; Livneh et al., 2020; Samuelsen et al., 2012). IC neurons are also involved in processing valence information, as activation of aIC neurons, for instance, produces positive valence and appetitive response (Peng et al., 2015; Wang et al., 2018). However, activation of aIC neurons can also produce negative valence and aversive response (Wu et al., 2020). Interestingly, inhibition of IC neurons (Contreras et al., 2007; Forget et al., 2010), or specific inhibition of aIC neurons (Venniro et al., 2017), reduces addictive behaviors, suggesting that the rodent IC is also critical for motivation, like its counterpart in humans. Nonetheless, given that learning, valence, and motivation are dissociable processes (Berke, 2018; Berridge et al., 2009; Mohebi et al., 2019; Shuvaev et al., 2020), it is unclear how the IC orchestrates such divergent functions, and how the IC controls motivation.

It is possible that the functional divergence is a manifestation of cell type heterogeneity. Indeed, studies on the IC have thus far targeted largely unspecified populations, which are highly heterogeneous (Dikecligil et al., 2020; Maffei et al., 2012). For projection neurons alone, there are hundreds of transcriptomic types (Tasic et al., 2018; Yao et al., 2021), with adjacent but transcriptionally distinct neurons having different connectivity (Chen et al., 2019; Matho et al., 2021; Zhang et al., 2021). Moreover, even neurons projecting to the same target can have opposing functions (Zhang et al., 2021). Therefore, neuronal type identity in combination with connectivity specificity may determine the functions of different insular populations.

In this study, we tested the hypothesis that aIC neurons projecting to the brainstem nucleus tractus solitarii (NTS) regulate motivational processes. The only cortical neurons that directly project to the brainstem are the large pyramidal tract (PT) neurons in layer 5B (Chen et al., 2019; Harris and Shepherd, 2015), which have distinct genetic identity, connectivity, and physiological properties compared with neighboring neurons (Harris and Mrsic-Flogel, 2013; Harris and Shepherd, 2015; Matho et al., 2021; Suter et al., 2013). Therefore, we used a genetic strategy combined with viral tools to target aIC PT neurons, as well as neurons along the aIC→NTS circuit. This approach allowed us to pinpoint highly specific functions of this circuit in motivational control.

RESULTS

The input and output connections of aIC^{Fezf2} neurons

As PT neurons are specified by the master transcription factor Fezf2 (forebrain expressed zinc finger 2) (Harris and Shepherd, 2015; Lodato et al., 2014), we used a *Fezf2-CreER* knock-in mouse driver – which expresses the inducible Cre recombinase (CreER) under the control of endogenous *Fezf2* promoter – to target PT neurons in the aIC. We injected

the aIC of *Fezf2-CreER* mice with an adeno-associated virus (AAV) expressing GFP in a Cre-dependent manner (Figure S1A), followed by tamoxifen induction. We observed dense axon fibers originating from the labeled aIC PT neurons – hereafter referred to as aIC^{Fezf2} neurons – in brainstem areas (including the NTS and parabrachial nucleus (PBN)) and the thalamus (Figure S1B–F). There were also moderate to sparse fibers in forebrain areas, including the striatum, parasubthalamic nucleus, amygdala and posterior IC (Figure S1G–K).

To examine the afferents of aIC^{Fezf2} neurons, we specifically infected these neurons with a rabies virus system (Figure S1L, M), which revealed that aIC^{Fezf2} neurons receive prominent monosynaptic inputs from various sources, including the motor, somatosensory and prefrontal cortices, and insula itself (Figure S1N, O, V); these neurons also receive strong inputs from the basolateral amygdala, thalamus, olfactory areas, hippocampal formation (Figure S1P–S, V), and midbrain and hindbrain areas, especially the dorsal raphe nucleus and PBN (Figure S1T–V).

aIC^{Fezf2} neurons represent motivational vigor

Next, we characterized the *in vivo* response properties of aIC^{Fezf2} neurons. We infected these neurons with the genetically encoded calcium indicator GCaMP6 (Chen et al., 2013), and implanted a gradient-index (GRIN) lens into the aIC (Figure 1A; Figure S2A). This approach allowed imaging aIC^{Fezf2} neuron activities – represented as GCaMP6 signals – at cellular resolution through the GRIN lens in behaving mice (Figure 1B; Video S1).

We first examined how individual neurons responded to sweet and bitter tastes by providing the mice with sucrose and quinine solutions. Many neurons were excited, while others were inhibited during consumption of the two liquids (Figure S2B, C), with the excited and inhibited neurons intermingled with no obvious spatial clustering (Figure S2D, E). Notably, a large population was excited by both sucrose and quinine, while another population was inhibited by both tastants (Figure S2B, C, F). As mice's licking rate exhibited apparent variability across trials (Figure 1C), a phenomenon known to reflect fluctuating motivation (Berditchevskaia et al., 2016), we examined if this variability was reflected in neural activity. Remarkably, the responses of a substantial fraction of neurons (~40% of 369 neurons imaged in 5 mice) scaled up or down with the licking rates during consumption (Figure 1D, E). Indeed, the neuronal response amplitudes showed either positive or negative trial-by-trial correlations with licking rates, regardless of whether the sucrose or quinine solution was consumed (Figure 1F, G; Figure S2G). In contrast, during baseline period (when liquid was unavailable), the activity of only few (~8.67%) of these neurons was correlated with mice's spontaneous licking (Figure S2H). These results suggest that a major population of aIC^{Fezf2} neurons represent the strength or vigor of licking, rather than taste or the movement associated with licking.

If aIC^{Fezf2} neurons represent action vigor, then their response should be dependent upon animal's motivational state. To test this prediction, we trained these mice in a reward-seeking task, in which a sound (conditioned stimulus, CS) predicted that a liquid reward (unconditioned stimulus, US) would be delivered, but only if the mice licked the spout during a response window following the CS (Figure 1H, L, P). We imaged the CS- and

US-evoked responses of aIC^{Fezf2} neurons while the mice transitioned between low and high levels of motivational drive under three distinct conditions. First, mice were kept thirsty and trained to lick for the delivery of a sucrose solution (Figure 1H). Well-trained thirsty mice showed increased anticipatory licking upon CS presentation; however, after free drinking was provided, the CS could no longer evoke licking, indicating that the mice were quenched (Figure 1I). We imaged aIC^{Fezf2} neuron activity across thirsty and quenched states (Figure S2I, J). When the mice were thirsty, a substantial population of neurons responded to the CS, with one subset showing excitation and the other showing inhibition (Figure 1J; Figure S2I, J). Interestingly, both the excitatory and inhibitory responses followed characteristic ramping trajectories, starting from CS onset and reaching a peak or trough, respectively, upon US delivery (Figure 1J; Figure S2J). However, such responses completely disappeared once the mice were quenched (Figure 1J, K; Figure S2I, J).

Second, the mice were kept thirsty and learned that the CS predicted a small drop (3 μl) of sucrose in one block, but the same CS predicted a large drop (12 μl) of sucrose in another block of trials (Figure 1L, M). We imaged the activity of aIC^{Fezf2} neurons across the two blocks (Figure S2K–M), which presumably engaged with different levels of motivation. In both blocks, many neurons showed either excitatory or inhibitory response to the CS, but the response in the large-reward block was much larger than that in the small-reward block (Figure 1N, O; Figure S2K, L). However, the CS-evoked licking was comparable in the two blocks, although the US-evoked licking in the large-reward block was more vigorous (Figure 1M; Figure S2M). These results suggest that aIC^{Fezf2} neuron response reflects alterations in motivation levels preceding the occurrence of apparent motor changes.

Third, the mice were subject to a sodium-deficiency condition (Lee et al., 2019; Tindell et al., 2009) and learned that CS predicted the delivery of a high-sodium solution (500 mM NaCl; Figure 1P), which is repellent to animals under normal conditions. The mice readily licked the spout following CS presentation (Figure 1Q), reflecting a homeostatic need for sodium. As expected, the mice stopped responding to the CS after recovery from the deficiency (Figure 1Q). Remarkably, under sodium-deficiency, many aIC^{Fezf2} neurons showed robust excitatory (27%) or inhibitory (29%) responses to sodium or the CS predicting sodium delivery, which were completely abolished after the mice had recovered from the deficiency (Figure 1R, S; Figure S2N, O).

To determine if the same neurons are involved in processing changing homeostatic demands, we tracked individual neurons across thirsty (Figure 1H) and sodium-deficiency (Figure 1P) states. Among the traceable neurons, a large fraction of those excited by sucrose solution when mice were thirsty (10 out of 18) were also excited by high-sodium when the mice were under sodium-deficiency (Figure S2P).

These results show that aIC^{Fezf2} neuron response is potently modulated by action vigor, homeostatic demand and the values of expected outcomes. In particular, these neurons represent the anticipation of outcomes that meet the changing needs of animals, even if the outcome – such as the high-sodium – is expected to be unpleasant. Thus, aIC^{Fezf2} neurons integrate the learned, predictive signals with the information about homeostatic needs to represent anticipation and motivational vigor.

The anticipation response emerges during learning

To further investigate how aIC^{Fezf2} neurons acquire anticipatory signals and participate in establishing motivated actions, we sought to image the activity of these neurons during learning in a "go/no-go" task (Figure 2A). In the "Go" trials of this task, a sound (CS_{SU}) indicated that sucrose would be delivered, but only if mice licked the spout during a decision window ("hit"). In the "No-go" trials, another sound (CS_{QU}) announced that quinine would be delivered, but mice could avoid it by withholding licking in the decision window ("correct rejection (CR)"; Figure 2A).

We imaged the activity of aIC^{Fezf2} neurons at different stages of training (Figure 2B–D; Figure S2Q). By examining the activity of all the neurons in hit and CR trials, we found that initially very few neurons responded to CS; however, training dramatically increased the neurons showing excitatory response to CS_{SU}, and had a trend to increase the neurons showing inhibitory response to CS_{SU} (Figure 2E, F; Figure S2R, S). Training also increased sucrose-responsive neurons, especially those showing inhibitory response (Figure 2E, F). Very few neurons responded to CS_{QU} throughout training (Figure 2E).

Interestingly, training markedly increased the number of neurons responsive to both CS_{SU} and sucrose (excitation, $P = 2.03 \times 10^{-10}$, inhibition, $P = 2.62 \times 10^{-5}$, χ^2 test; Figure 2F). Consistent with this observation, population analysis revealed that training led to an increase in similarity between the response to CS_{SU} and sucrose, quantified as a decrease in Mahalanobis distance between the ensemble representations of the two stimuli (Figure 2G). These results indicate that training fundamentally modifies the responsiveness of aIC^{Fezf2} neurons, such that the response to the reward cue becomes matched with that to the actual reward.

To further examine how the response of aIC^{Fezf2} neurons evolves during learning, we projected their population activity along the axes that optimally separated the anticipatory response in different trial types (Figure S2T). Robust predictive and ramping signals developed during training, such that the hit and CR trials became better separated at the late than early stage (Figure S2T). Consistently, training increased the difference between CS ensemble representations in hit and CR trials (Figure S2U, V). Furthermore, the CS population response can be used to decode Go and No-go trials, with decoding accuracy dependent on learning (Figure S2W, X). These results suggest that learning induces robust anticipatory response in aIC^{Fezf2} population, which is specific for reward and can be used to instruct or invigorate reward-seeking behavior.

The anticipation response precedes actions and correlates with action strength

If aIC^{Fezf2} neurons act to invigorate behaviors, then their anticipatory activities are expected to occur earlier than, correlate with, and be required for motivated behaviors. To test these predictions, we first examined the relationship between neuronal and behavioral response in the reward-seeking task or the go/no-go task, during the time window when thirsty or sodium-depleted mice were anticipating sucrose or NaCl solution, respectively (Figure 1L, P; Figure 2A). Indeed, timing analysis revealed that most CS-excited neurons responded earlier than licking onset (Figure S3A & B, E & F, I & J). Furthermore, trial-by-trial analysis

showed that the response amplitudes of major aIC^{Fezf2} populations correlated with licking rates (Figure S3C & D, G & H, K & L). These results are consistent with the notion that aIC^{Fezf2} neurons may provide signals that motivate or invigorate reward-seeking actions.

aIC^{Fezf2} anticipatory activity is required for motivational actions

Next, to determine the causal relationship between aIC^{Fezf2} neurons and motivational actions, we sought to specifically inhibit these neurons during anticipation with optogenetics (Figure 2H–Q). For this purpose, we expressed a light-sensitive neuronal inhibitor GtACR2 (Govorunova et al., 2015; Mahn et al., 2018), or mCherry (as a control), selectively in aIC^{Fezf2} neurons, and implanted optical fibers above the infected areas for light delivery (Figure 2H, I). These mice were subsequently trained in the go/no-go task (Figure 2A). At the late stage of training, we delivered blue light into the aIC during the time window between CS onset and US onset, in randomly selected trials (Figure 2J–L).

Strikingly, the photostimulation in the GtACR2 mice caused a dramatic reduction in anticipatory licking in Go trials, resulting in decreased hit rate (Figure 2J–L). These mice were not affected by the laser in No-go trials, but this was because licking was rare in these trials to begin with. As expected, the mCherry mice were not affected by the laser in either Go or No-go trials (Figure 2L). Interestingly, once the GtACR2 mice had started licking in a “continuous licking” task, the photostimulation had no effect on the on-going licking behavior (Figure 2M, N). Thus, inhibiting aIC^{Fezf2} neurons impairs the anticipatory licking needed for obtaining reward, but does not affect the motor program underlying licking behavior.

To determine if aIC^{Fezf2} neurons are required specifically for licking, or generally for reward-seeking actions, we designed a “run-for-reward” (RFR) task in which mice needed to run upon CS presentation to obtain water reward (Stephenson-Jones et al., 2020) (Figure 2O). Once mice learned the task, we optogenetically inhibited aIC^{Fezf2} neurons during the window between CS onset and US onset in randomly selected trials (Figure 2O). This manipulation markedly reduced running velocity, leading to reduced performance in this task (Figure 2P, Q). Again, laser illumination in the aIC had no effect on the mCherry mice (Figure 2Q). Thus, aIC^{Fezf2} neurons are essential for promoting running to obtain reward.

We also examined whether inhibiting aIC^{Fezf2} neurons could influence valence processing, general body movements, or consumption. We found that, in a real-time place preference or aversion (RTPP/A) test, inhibition of aIC^{Fezf2} neurons did not cause preference or aversion; neither did it affect animals’ movement (Figure S4A–E). In addition, inhibiting aIC^{Fezf2} neurons did not affect *ad libitum* sucrose consumption (Figure S4F, G).

Together, these results indicate that aIC^{Fezf2} neuron activity is required for the volitional aspect of reward-seeking actions, but is dispensable for motor functions or consumption.

aIC^{Fezf2}→NTS activation invigorates motivational licking

aIC^{Fezf2} neurons send dense projections to the NTS (Figure S1A, B), consistent with previous observations that the IC sends long-range direct projections to the NTS (Jin et al., 2021; Shipley, 1982). Therefore, we tested if the functions of aIC^{Fezf2} neurons we

observed are conveyed through aIC^{Fezf2}→NTS pathway. We first examined the composition of aIC projections to the NTS. More than 90% of NTS-projecting aIC neurons were *Fezf2*-expressing (*Fezf2*$^{+}$) (Figure 3A–D), demonstrating that aIC→NTS projections originate predominately from aIC^{Fezf2} neurons.

We then probed aIC^{Fezf2}→NTS function with optogenetics. To this end, we bilaterally infected aIC^{Fezf2} neurons with an AAV expressing the light-gated cation channel ChR2, or GFP, and implanted optical fibers in the NTS above the axons originating from the infected neurons (Figure 3E, F). These mice underwent training in the go/no-go task (Figure 3G). At the late stage of training, we delivered blue light pulses into the NTS during the window between CS onset and US onset in randomly selected trials (Figure 3E–H).

Remarkably, the photostimulation in the ChR2 mice caused an increase in licking rate following CS presentation in not only Go trials, but also No-go trials (Figure 3H, I). As a result, the CR rate was reduced; the hit rate was increased, although without reaching significance due to a ceiling effect (P = 0.09; Figure 3J). Interestingly, before training in the task, the photostimulation did not induce any licking following either the Go or the No-go tone, even though the mice were thirsty (Figure 3K). Moreover, after these mice were well trained but quenched, the photostimulation also failed to promote licking in the task (Figure 3L). The GFP mice were not affected by the laser (Figure 3J). These results suggest that aIC^{Fezf2} →NTS activity invigorates the learned, anticipatory licking response to obtain a homeostatic need; however, it does not override satiety signals or autonomously activate the motor program to generate licking.

aIC^{Fezf2}→NTS promotes vigor and effort

To determine if aIC^{Fezf2}→NTS is only involved in licking, we trained mice to perform the RFR task described above (Figure 2O), and optogenetically activated their aIC^{Fezf2}→NTS during the anticipation window (Figure 3M–P). This manipulation markedly increased the velocity of anticipatory running, and led to improved performance (Figure 3M, N). However, the same manipulation did not promote running before these mice were trained in the task (Figure 3O); it also failed to promote anticipatory running after the same mice were fully trained but quenched (Figure 3P). Laser illumination in the NTS had no effect on the GFP mice (Figure 3N). Thus, the results in the RFR and go/no-go tasks together demonstrate that aIC^{Fezf2}→NTS activity is capable of promoting different forms of volitional actions, on the condition that such actions have been learned and the outcome is homeostatically needed. In other words, aIC^{Fezf2}→NTS activity invigorates “need seeking”, but does not override homeostasis or automatically lead to action generation.

Next, we tested mice in a progressive-ratio (PR) task (Figure 3Q–U). In this task, the effort required for thirsty mice to attain water increased progressively, and the breakpoint at which the mice stopped responding was used as a measure of motivation (Figure 3Q). In some sessions, we optogenetically activated aIC^{Fezf2}→NTS. This manipulation significantly increased the breakpoint and the total number of reward-seeking actions (Figure 3R–U). Thus, aIC^{Fezf2}→NTS activation promotes the effort an animal spends in pursuing reward.

Notably, we found that optogenetically activating this pathway did not induce appetitive (or aversive) responses, neither did it affect animals' locomotion in the RTPP/A test (Figure S4H–L). Activating this pathway also failed to support self-stimulation (Figure S4M–O). To test whether aIC^{Fezf2}→NTS activation promotes consumption, we activated the aIC^{Fezf2}→NTS pathway in hungry or thirsty mice in the presence of food or water, respectively. The activation did not increase food or water intake (Figure S4P, Q). In a separate test, activating this pathway also did not affect *ad libitum* sucrose consumption (Figure S4F, R). These results show that aIC^{Fezf2}→NTS activity does not produce valence, affect movement, or influence food and liquid consumption.

Together, these results strongly suggest that aIC^{Fezf2}→NTS carries out the invigoration function of aIC^{Fezf2} neurons and promotes the effort of motivational actions.

The dependence on the perceived value

Next, we systematically examined the effects of aIC^{Fezf2}→NTS activation in well-trained mice performing the reward-seeking task (Figure 4A–G). We found that in a quenched state, activating aIC^{Fezf2}→NTS did not induce anticipatory licking that would lead to water delivery (Figure 4A–C; F & G, leftmost). In contrast, in a thirsty state, activating this pathway dramatically increased the rate of anticipatory licking for either water or a sucrose solution, and even for a NaCl solution (300 mM), albeit to a lower level (Figure 4D, F). As a result, the performance in these sessions was improved (Figure 4G). The activation also potently promoted anticipatory licking for Ensure (a liquid food) when the mice were hungry (Figure 4E; F & G, rightmost). However, the activation failed to increase anticipatory licking in sessions in which quinine was the US, or when no US was delivered (i.e., in extinction), even if the mice were thirsty (Figure 4D, F, G). These results thus confirm that aIC^{Fezf2}→NTS function depends on homeostatic needs, and further suggest that it depends on the perceived values of outcomes under on-going homeostatic demands.

The aIC^{NTS} subpopulation is enriched with anticipation signals

To monitor the endogenous function of aIC^{Fezf2}→NTS pathway, we selectively imaged the activity of the NTS-projecting subpopulation of aIC^{Fezf2} neurons. As essentially all NTS-projecting neurons in the aIC (aIC^{NTS}) are *Fezf2*$^{+}$ (Figure 3A–D), we labelled aIC^{NTS} neurons with GCaMP6 for the imaging, by injecting the NTS of wild-type mice with a retrograde AAV expressing Cre, and injecting the aIC of the same animals with the AAV expressing GCaMP6 Cre-dependently (Figure 5A). We imaged the activity of aIC^{NTS} neurons as we did for aIC^{Fezf2} neurons (Figure 5A, B).

Like aIC^{Fezf2} neurons, aIC^{NTS} neurons showed excitatory or inhibitory response to sucrose and quinine, which scaled up or down with mice's licking rates (Figure S5A–C). Moreover, the response amplitudes of many neurons showed positive or negative correlations with the licking rates during liquid consumption (Figure S5D, E), but not during baseline periods (Figure S5F). Interestingly, compared with aIC^{Fezf2} neurons, a much larger fraction of aIC^{NTS} neurons showed excitatory response to sucrose (aIC^{NTS}, 34.5%; aIC^{Fezf2}, 19.5%), or to both sucrose and quinine (aIC^{NTS}, 14%; aIC^{Fezf2}, 8.4%) (Figure S5G, H).

In the reward-seeking task in which the size of reward was variable, the anticipatory response – either excitatory or inhibitory – of many aIC^{NTS} neurons in big-reward trials was larger than that in small-reward trials (Figure 5C–G). Furthermore, the anticipatory neuronal response preceded and correlated with mice's licking action (Figure 5H–K). Notably, compared with aIC^{Fezf2} neurons imaged in the same task (Figure S3D), a much greater fraction of aIC^{NTS} neurons showed such correlative responses (aIC^{NTS}, 79.2%; aIC^{Fezf2}, 36%) (Figure 5L). In addition, although the anticipatory response of either aIC^{Fezf2} or aIC^{NTS} could be used to classify between small- and big-reward trials, aIC^{NTS} was better in decoding performance (Figure 5M). These results together indicate that the aIC^{NTS} subpopulation is more enriched with the anticipation or vigor signals than the larger aIC^{Fezf2} population, and thus may convey these signals to the NTS.

Anticipation signals emerge in $NTS^{Recipient}$ neurons during learning

To determine whether the anticipation signals in aIC^{Fezf2} or aIC^{NTS} neurons are conveyed to the NTS, we monitored the activity of the NTS neurons receiving direct synaptic inputs from the aIC – termed $NTS^{Recipient}$ neurons. To target $NTS^{Recipient}$ neurons, we bilaterally injected the aIC of wild-type mice with an anterograde transsynaptic AAV1-Cre (Zingg et al., 2017), and injected the NTS of the same animals with the Cre-dependent GCaMP6 AAV (Figure S5I, J). Optical fibers were subsequently implanted into the NTS, above the infected $NTS^{Recipient}$ neurons (Figure S5I, J).

We recorded the bulk activities of $NTS^{Recipient}$ neurons in these mice with fiber photometry, at different stages of training in the go/no-go task (Figure S5K–M). At the early stage of training, $NTS^{Recipient}$ neurons showed little response following CS presentations in either the Go or No-go trials (Figure S5N, O, R). However, at the late stage, these neurons displayed ramping-up activities following CS presentations till sucrose was delivered in the Go trials (Figure S5P–S). In contrast, such anticipatory response was absent in the No-go trials. Thus, the anticipation response of $NTS^{Recipient}$ neurons, which bears characteristics of that of aIC^{Fezf2} neurons, emerges during learning, paralleling the establishment of need-seeking behavior.

$NTS^{Recipient}$ activity is required for need-seeking actions

To determine if the anticipatory activity of $NTS^{Recipient}$ neurons is required for need-seeking behavior, we specifically inhibited these neurons during anticipation in mice performing the go/no-go task (Figure 6A–E). Strikingly, this manipulation caused a dramatic decrease in the anticipatory licking in Go trials, resulting in impaired performance (Figure 6C–E). In contrast, the inhibition had no effect on the on-going licking behavior in the continuous licking task (Figure 6F, G).

Furthermore, in the RFR task, inhibition of $NTS^{Recipient}$ neurons during anticipation markedly reduced the anticipatory running and performance (Figure 6H, I). However, inhibiting these neurons did not induce aversion or preference, or any change in movement in the RTPP/A test (Figure S4S–W); it also did not affect *ad libitum* sucrose consumption (Figure S4F, X). Together, these results demonstrate that $NTS^{Recipient}$ activity is essential for

the anticipatory control of different forms of goal-directed actions, but dispensable for motor function or consumption.

aIC^{Fezf2}→NTS promotes dopamine release when the outcome is needed

To map the downstream targets that may mediate the function of NTS^{Recipient} neurons, we labelled these neurons with GFP (Figure S6A, B). Notably, we found dense GFP-labelled axon fibers in dopamine areas including the retrorubral field (RRF) – which is populated by the A8 dopaminergic neuron group (Figure S6C) (Fu et al., 2012) – and the visual tegmental relay zone (VTRZ), a brain region located next to the ventral tegmental area (VTA) (Figure S6D). In both areas the axon fibers were in close proximity to dopamine neurons (Figure S6C, D). Axon fibers were also observed in the thalamus (Figure S6E) and PBN (Figure S6F). Thus, NTS^{Recipient} neurons can potentially influence dopamine neuron function through their direct projections to the RRF or VTRZ, or through an indirect pathway via the PBN (Figure S6G).

Dopamine signalling in the nucleus accumbens (NAc) is involved in the modulation of action vigor (du Hoffmann and Nicola, 2014; Hamid et al., 2016; Ko and Wanat, 2016; Mohebi et al., 2019). Therefore, we examined whether aIC^{Fezf2}→NTS can regulate NAc dopamine release. We bilaterally expressed ChR2 in aIC^{Fezf2} neurons, and also expressed a genetically encoded dopamine sensor DA2m (Sun et al., 2018; Sun et al., 2020) in NAc neurons of the same mice. Optical fibers were subsequently implanted in the NTS and NAc, for photostimulation and fiber photometry, respectively (Figure 7A, B).

We trained these mice to perform the go/no-go task while recording dopamine release in the NAc with photometry. In randomly selected trials, we moderately photostimulated aIC^{Fezf2}→NTS during the anticipation period (Figure 7C, D). In the absence of the stimulation (“no laser”), dopamine release increased and decreased following CS in Go and No-go trials, respectively (Figure 7E–I). Interestingly, the stimulation (“laser”) further enhanced the increase in dopamine release in Go trials, and prevented the decrease in dopamine release in No-go trials (Figure 7E, G, I).

The observed enhancement of dopamine release was unlikely secondary to an increase in licking, as activating aIC^{Fezf2}→NTS did not affect licking in no-go trials, but still enhanced dopamine release (Figure 7H, I). Furthermore, we selected “no-laser” and “laser” Go trials with similar anticipatory licking rates (Figure 7J; Methods). Analysis on such licking rate-matched Go trials still showed that aIC^{Fezf2}→NTS activation was accompanied by an increase in dopamine release (Figure 7K, L). In the GFP control mice, shining light in the NTS had no effect (Figure 7M, N).

Finally, we repeated the activation when the mice were quenched, which failed to affect dopamine release in either Go or No-go trials (Figure 7O–Q). These results together indicate that aIC^{Fezf2}→NTS promotes dopamine release in the NAc, but only when the outcome is homeostatically needed.

DISCUSSION

Features of the aIC^{Fezf2}→NTS circuit

The aIC^{Fezf2}→NTS circuit exhibited several distinctive features. First, aIC^{Fezf2}→NTS function strictly depended upon homeostatic needs. Thus, this circuit does not mediate the conventional reward-seeking function, which typically drives positive reinforcement and overconsumption (Berridge et al., 2009). Rather, it carries out a “need-seeking” function that is engaged only when a goal is homeostatically needed. Second, the response of a large fraction of aIC^{Fezf2} or aIC^{NTS} neurons did not represent sweet or bitter taste. Third, aIC^{Fezf2}→NTS only invigorated learned actions, but did not influence movement per se. Fourth, a stable set of aIC^{Fezf2} neurons participated in processing changing homeostatic needs. Our results altogether suggest that the aIC^{Fezf2}→NTS circuit constitutes a common neural substrate that integrates learned, predictive signals with the information about fluctuating homeostatic needs to encode and regulate the motivational vigor of need-seeking behaviors.

Perspectives

Our results that inhibition or activation of neurons along the aIC^{Fezf2}→NTS pathway potently suppresses or heightens, respectively, motivational vigor without influencing food or fluid consumption, or affecting valence processing indicate that the function of this circuit is remarkably specialized. These results provide plausible explanations for the observations that patients with insular lesions have reduced motivational vigor or decreased addictive behaviors, but have normal food intake and the pleasure of eating (Manes et al., 1999; Naqvi et al., 2014; Naqvi et al., 2007). Given that vigor is a core manifestation of motivation (Niv et al., 2007; Rigoli et al., 2016), our results also provide insights into the aIC dysfunctions linked with mood and motivational disorders (Etkin, 2010; Mutschler et al., 2019; Paulus and Stein, 2010; Sliz and Hayley, 2012; Sprengelmeyer et al., 2011; Stratmann et al., 2014). We propose that regulating activity in the nodes along aIC→NTS circuit could be a viable approach to achieve bidirectional and precise control of vigor and effort, and hence this circuit represents a potential therapeutic target for treating vigor- or effort-related symptoms prevalent among individuals affected by depression or drug addiction.

Limitations of the study

Our *in vivo* imaging results revealed the existence of two distinct functional types among aIC^{Fezf2} or aIC^{NTS} neurons, with one exhibiting excitatory response and the other showing inhibitory response during the anticipation and consumption of homeostatically needed substances. However, our optogenetic manipulation did not discriminate between these two types, and especially did not unravel the role of the neurons with inhibitory response. The recently developed technologies for simultaneous optogenetics and imaging at single-cell resolution (Emiliani et al., 2015) may prove to be useful in addressing this issue.

STAR Methods

RESOURCE AVAILABILITY

Lead Contact—Further information and requests for resources and reagents should be directed to and will be fulfilled by the Lead Contact, Bo Li (bli@cshl.edu).

Materials Availability—This study did not generate new unique reagents.

Data and code availability

- The authors declare that the data supporting the findings of this study are available within the paper and its supplementary information files.
- All original code has been deposited at Figshare and is publicly available as of the date of publication. DOIs are listed in the key resources table.
- Any additional information required to reanalyze the data reported in this paper is available from the lead contact upon request.

EXPERIMENTAL MODEL AND SUBJECT DETAILS

Male and female mice (2–4 months old) were used for all the experiments. All mice were bred onto a C57BL/6J background. Mice were housed in groups of 2–5 under a 12 h light/dark cycle (8 a.m. to 8 p.m. light), with food and water available *ad libitum* before being used for experiments. All behavioral experiments were conducted during the light cycle. Littermates were randomly assigned to different groups prior to experiments. All experimental procedures were approved by the Institutional Animal Care and Use Committee of Cold Spring Harbor Laboratory (CSHL) and performed in accordance to the US National Institutes of Health guidelines in an AAALACi accredited facility.

The *Fezf2-CreER* knock-in (Matho et al., 2021) and *H2B-GFP* (*Rosa26-stop*^{flox}*-H2B-GFP*) reporter (He et al., 2012) mouse lines were generated by Z. Josh Huang's lab at CSHL.

METHOD DETAILS

Immunohistochemistry—Immunohistochemistry experiments were performed following standard procedures described previously (Xiao et al., 2020). Briefly, mice were anesthetized with Euthasol (0.2 ml; Virbac, Fort Worth, Texas, USA) and transcardially perfused with 30 ml PBS, followed by 30 ml 4% paraformaldehyde (PFA) in PBS. Brains were extracted and further fixed in 4% PFA overnight followed by cryoprotection in a 30% PBS-buffered sucrose solution for 36–48 h at 4 °C. Coronal sections (50 μm) were cut using a freezing microtome (Leica SM 2010R, Leica). Sections were first washed in PBS (5 min), incubated in PBST (0.3% Triton X-100 in PBS) for 30 min at room temperature (RT) and then washed with PBS (3 × 5 min). Next, sections were blocked in 5% normal goat serum in PBST for 30 min at RT and then incubated with primary antibodies overnight at 4 °C. Sections were washed with PBS (3 × 5 min) and incubated with fluorescent secondary antibodies at RT for 2 h. In some experiments (as indicated in Figures and Supplementary Figures), sections were washed twice in PBS, incubated with DAPI (4′,6-diamidino-2-phenylindole, Invitrogen, catalogue number D1306)

(0.5μg/ml in PBS) for 2 min. After washing with PBS (3 × 5 min), sections were mounted onto slides with Fluoromount-G (eBioscience, San Diego, California, USA). Images were taken using an LSM 780 laser-scanning confocal microscope (Carl Zeiss, Oberkochen, Germany). The primary antibodies used were: chicken anti-GFP (Aves Labs, catalogue number GFP1020; dilution 1:1000), rabbit anti-RFP (Rockland, catalogue number 600–401-379; dilution 1:1000), rabbit anti-tyrosine hydroxylase (TH) (Millipore, catalogue number AB152; dilution 1:1000). Appropriate fluorophore-conjugated secondary antibodies (Life Technologies) were used depending on the desired fluorescence colors.

Viral vectors—The following adeno-associated viruses (AAVs) were produced by the University of North Carolina vector core facility (Chapel Hill, North Carolina, USA): AAV5-Ef1a-DIO-hChR2(H134R)-eYFP, AAV9-CAG-Flex-GFP. The AAV1-Syn-Flex-GCaMP6f-WPRE-SV40, AAV1-hSyn-SIO-stGtACR2-FusionRed and AAV-Ef1a-mCherry-IRES-Cre (retrograde) (Fenno et al., 2014) were produced by Addgene (Watertown, MA, USA). The AAV1-hSyn-Cre-WPRE-hGh (anterograde trans-synaptic) was packaged by UPenn Vector Core (Philadelphia, PA, USA). The AAV9-hSyn-DA2m was packaged by Vigene Biosciences (Rockville, MD, USA). The following viruses, which are components of the rabies viral tracing system, were produced by HHMI Janelia Research Campus: AAV2/9-CAG-Flex-mKate-T2A-TVA, AAV2/9-CAG-Flex-mKate-T2A-N2c-G, Rbv-CVS-N2c-ΔG-GFP (the modified rabies virus). All viral vectors were aliquoted and stored at −80 °C until use.

Stereotaxic surgery—All surgery was performed under aseptic conditions and body temperature was maintained with a heating pad. Standard surgical procedures were used for stereotaxic injection and implantation as previously described (Xiao et al., 2020). Briefly, mice were anesthetized with isoflurane (1–2% in a mixture with oxygen, applied at 1.0 L/min), and head-fixed in a stereotaxic injection frame, which was linked to a digital mouse brain atlas to guide the targeting of different brain structures (Angle Two Stereotaxic System, myNeuroLab.com). Lidocaine was injected subcutaneously into the head and neck area as a local anesthetic.

We first made a small cranial window (1–2 mm^2) above the target brain region. To prepare mice for the GRIN lens imaging experiments, we lowered a glass micropipette (tip diameter, ~5 μm) containing the AAV1-Syn-Flex-GCaMP6f-WPRE-SV40 viral solution to reach the aIC at two dorsoventral positions (coordinates: 1.6 mm anterior to Bregma, 3.1 mm lateral from midline, 1.9 mm and 2.1 mm vertical from brain surface). About 0.25 μl of viral solution was delivered at each injection site (in total 0.5 μl) with pressure applications (5–20 psi, 5–20 ms at 1 Hz) controlled by a Picospritzer III (General Valve) and a pulse generator (Agilent). The rate of injection was ~20 nl/min. The pipette was left in place for 10 min following the injection, and then slowly withdrawn. In the experiment to image NTS-projecting aIC (aIC^{NTS}) neurons, we additionally injected the AAV-Ef1a-mCherry-IRES-Cre (retrograde) into the NTS (coordinates: 6.55 mm posterior to Bregma, 1.37 mm lateral from midline, and 3.8 mm vertical from brain surface). One week later, we performed the second surgery to implant a GRIN lens (diameter, 0.6 mm; length, 7.3 mm; Inscopix). The lens was slowly (~100 μm/min) lowered to the aIC (coordinates: 1.6 mm anterior to Bregma, 3.1

mm lateral from midline, 1.7 mm vertical from brain surface), and subsequently secured to the skull by using C&B-Metabond (Parkell, catalogue number S380). A metal head-bar (for head restraint) was then mounted onto the skull with black dental cement (Ortho-Jet). We waited for ~4 weeks before starting the imaging experiments in these mice.

To prepare mice for the optogenetic experiments, we first injected the targets in both hemispheres with viruses, and subsequently implanted optic fibers above the injection locations or axon terminal fields. A head-bar was also mounted for head restraint. Viruses were injected at a volume of ~0.3 μl at each site, and were allowed ~4 weeks for expression. Viral injection was performed at the following stereotaxic coordinates for the aIC: 1.6 mm anterior to Bregma, 3.1 mm lateral from midline, 2.0 mm ventral from cortical surface; NTS: 6.55 mm posterior to Bregma, 1.37 mm lateral from midline, 3.8 mm ventral from cortical surface. Coordinates for optic fiber implantation were as follows: aIC: 1.6 mm anterior to Bregma, 3.1 mm lateral from midline, 1.65 mm ventral from cortical surface; NTS: 6.55 mm posterior to Bregma, 1.5 mm lateral from midline, 3.6 mm ventral from cortical surface with a 3° angle; and PBN: 5.3 mm posterior to Bregma, 1.9 mm lateral from midline, 2.2 mm ventral from cortical surface with a 14.85° angle. The optic fibers (core diameter, 200 μm; length, 3 mm (for aIC and PBN) or 4.5 mm (for NTS); NA, 0.22; Newdoon, Hangzhou, China; or Inper, Hangzhou, China) used for the photostimulation transmitted light with >90% efficiency when tested before implantation.

To monitor the neural activity of NTS neurons receiving inputs from aIC (the $NTS^{Recipient}$) using fiber photometry, we injected the aIC with ~0.3 μl of the anterograde trans-synaptic AAV1-hSyn-Cre-WPRE-hGh, and injected the NTS with ~0.3 μl of AAV1-Syn-Flex-GCaMP6f-WPRE-SV40 at the coordinates described above. An optic fiber (core diameter, 200 μm; length, 4.5 mm; NA, 0.37; Newdoon, Hangzhou, China; or Inper, Hangzhou, China) was inserted 0.2 mm above the injection site in the NTS.

For the *in vivo* opto-photometry experiment, *Fezf2-CreER* mice were injected with ~0.3 μl AAV5-Ef1a-DIO-hChR2(H134R)-eYFP into the aIC and ~0.3 μl AAV9-hSyn-DA2m into the NAc core (coordinates: 1.3 mm anterior to Bregma, 0.8 mm lateral from midline, 3.8 mm ventral from cortical surface). Optical fibers for photoactivation were implanted in the NTS at coordinates described above. Optical fibers for fiber photometry were implanted 0.2 mm above the injection site in the NAc.

To retrogradely label PBN- and NTS-projecting neurons in the IC of the same mice, we unilaterally injected ~0.2 μl CTB-555 solution (0.1% in PBS) into the PBN (coordinates: 5.3 mm posterior to Bregma, 1.9 mm lateral from midline, 2.63 mm ventral from cortical surface with a 14.85° angle) and ~0.2 μl CTB-647 solution (0.1% in PBS) into the NTS in C57BL/6J mice. Mice were sacrificed 5 days after the injection to allow retrograde labeling of projection neurons.

For anterograde tracing of aIC^{Fezf2} neurons, we unilaterally injected ~0.2 μl of AAV9-CAG-Flex-GFP into the aIC in *Fezf2-CreER* mice. For anterograde tracing of $NTS^{Recipient}$ neurons, ~0.3 μl of AAV1-hSyn-Cre-WPRE-hGh was injected into the aIC, and ~0.3 μl

of AAV9-CAG-Flex-GFP was injected into the NTS. We waited about 3–4 weeks before perfusing the mice.

Mapping monosynaptic inputs with pseudotyped rabies virus—Retrograde tracing of monosynaptic inputs onto aIC^{Fezf2} neurons was accomplished using a previously described method (Reardon et al., 2016; Xiao et al., 2020; Zhang et al., 2021). We first injected the aIC of *Fezf2-CreER* mice with a mixture of AAV-Flex-mKate-T2A-TVA and AAV-Flex-mKate-T2A-N2c-G (1:2 volume : volume ratio; ~0.3 μl in total) that express the following components in a Cre-dependent manner: a fluorescent reporter mKate, TVA (which is a receptor for the avian virus envelope protein EnvA), and the rabies envelope glycoprotein (G). Three weeks later, mice were injected in the same location with Rbv-CVS-N2c-ΔG-GFP (~0.3 μl), a rabies virus that is pseudotyped with EnvA, lacks the envelope glycoprotein, and expresses GFP. This rabies strain has been shown to have enhanced retrograde trans-synaptic transfer and reduced neurotoxicity (Reardon et al., 2016). Brain tissue was prepared one week after the rabies virus injection for histological examination. This method ensures that the rabies virus exclusively infects cells expressing TVA. Furthermore, complementation of the modified rabies virus with the envelope glycoprotein in the TVA-expressing cells allows the generation of infectious particles, which then can transsynaptically infect presynaptic neurons.

Tamoxifen induction—All *Fezf2-CreER* mice underwent tamoxifen induction to activate the Cre-dependent expression of genes of interest. Tamoxifen (Sigma-Aldrich, catalogue number T5648) was dissolved in corn oil at a concentration of 20 mg/ml, by constant shaking for 24 hours at room temperature in a container protected from light. Aliquots (1 ml each) were stored at 4 ℃. Tamoxifen induction was performed via intraperitoneal injection at a dose of 0.1 mg/g of body weight, once every 2 days for a total of 3 times. For virally driven gene expression, the first induction was performed one day after surgery. All mice were closely monitored throughout the course of tamoxifen injections and the post-injection period.

The reward-seeking task under distinct motivational states—Thirsty mice were trained to perform a reward-seeking task, in which a sound (CS, 1 s in duration) predicted that a 200-mM sucrose solution (US) would be available for the mice to consume from a spout, but only if the mice licked the spout during a response window (2 s in duration) following CS presentation. Such trials were counted as “hit” trials. To assess how changes in thirst state influence behavioral and neural activity, we first conducted one session of the imaging experiment on mice performing the task in a thirsty state. Each mouse acquired 8 μl of the sucrose solution in every hit trial. At the end of the first session, we provided each of the mice with 2 ml of the sucrose solution. We then conducted a second session of imaging on these mice (which were all quenched).

To assess how reward size affects behavioral and neural activity, we performed the imaging experiment on thirsty mice performing the task in two blocks of trials in each session. In one block, a big reward (12 μl of sucrose solution) was delivered in each hit trial; in the other block, a small reward (3 μl of sucrose solution) was delivered in each hit trial. The same

CS was used in both blocks. The sequence of the blocks was counterbalanced in different sessions.

To assess how sodium deficiency affects behavioral and neural activity, we induced a sodium-depletion state in the mice, and used a high concentration (500 mM) of NaCl solution instead of the sucrose solution as the US in the reward-seeking task. To induce the sodium-depletion state, furosemide (Sigma, catalogue number F4381) was administered to mice via intraperitoneal injection (50 mg /kg of body weight), as previously described (Lee et al., 2019; Tindell et al., 2009). The mice were subsequently placed on a sodium-deficient diet (Bio-serv, catalogue number F7730) and had free access to distilled water. These mice were trained to lick for the NaCl solution in the reward-seeking task. We conducted one session of imaging on these mice performing the task. Each mouse acquired 5 μl of the NaCl solution in every hit trial. After this experiment, the mice were allowed to recover for at least 4 days on a normal diet. We conducted a second session of imaging on these mice after the recovery.

Go/no-go task—Water restricted mice were trained in an auditory go/no-go task under head restraint, as previously described (Xiao et al., 2020). Training started with habituation, during which mice received water reward by licking the water spout (2 μl for each lick). No auditory stimulus was presented. Once mice reliably licked the spout (for 2–3 days), they were subjected to the go/no-go training that included “go trials” and “no-go trials”. In go trials, an auditory stimulus (the “go tone”, 1 s in duration) was delivered, followed by a delay period (the “response window”, 1 s duration in optogenetics experiments and 2 s duration in imaging experiments). Licking during the response window was rewarded with a drop (5 μl) of a 200-mM sucrose solution. In no-go trials, a different auditory stimulus (the “no-go tone”, 1 s) was delivered, followed by a response window (same duration as that in go trials). Licking during the response window resulted in the delivery of a drop (5 μl) of a 5-mM quinine solution. The go trials and no-go trials were randomly interleaved. During the inter-trial interval, brief suction (500 ms in duration) near the spout was applied to remove any residual solution from the previous trial. For analysis, trials were sorted into go trials and no-go trials. In the optogenetics experiments, trials were further sorted into laser-on and laser-off trials. Laser illumination was delivered during the time window from tone onset to US onset in 20% of randomly selected trials. The laser illumination was 10 mW measured at the tip of optic fibers. For optogenetic activation, the laser pulses were 20 Hz with a 10-ms pulse width. For optogenetic inhibition, continuous illumination was applied. A correct response during a go trial (“hit”) occurred when the mouse successfully licked the spout during the response window and subsequently received the sucrose. A correct response during a no-go trial (“correct rejection”) occurred when the mouse successfully withheld lick response during the response window and thus avoided the delivery of quinine. Licking in no-go trials (false alarm, FA) resulted in the delivery of quinine. The performance was quantified as hit rate (number of hits / number of go trials) and correct rejection rate (number of correct rejections / number of no-go trials). Behavioral d-prime (d') was computed as follows:

$$d' = norminv(P_{Hit}) - norminv(P_{FA})$$

where *norminv* is the inverse of the cumulative normal function. Values of Hit and FA rate were truncated between 0.01 and 0.99, setting the maximum d' to 4.65.

Run-for-reward task—This task was designed to train mice to actively run on a wheel to pursue reward. Mice were first habituated to running on a wheel under head-restraint for 2–4 days (one session per day, each lasting 30~45 min). Mice were subsequently subjected to training in which they were presented with a 1-s 3-kHz tone followed by a 1-s response window. If mice ran above a threshold speed (8 cm/s) during the response window, they would receive 8 μl of water delivered through a spout. Such trials were counted as "hit" trials. Otherwise mice would receive nothing. Mice were trained one session per day. The inter-trial interval was randomly variable between 10 to 16 s.

Progressive-ratio task—Water restricted mice were placed in a chamber equipped with a water port. Mice were first trained to poke into the port for water reward on a "fixed ratio 1" (FR1) schedule for 2 days, during which every nose-poke leads to a reward (5 μl of water). Following the FR1 training, the schedule was changed to FR4 for 2 days, which required the mice to poke the port 4 times with a maximal inter-poke-interval of 2 minutes in order to receive the reward. Next, the schedule was changed to FR10 for 1 day. Finally, mice were tested with a progressive ratio (PR) schedule in which the number of nose-pokes required to obtain one reward followed a geometric progression according to a function:

$$N_j = 20e^{j/20} - 20$$

where j is the trial number. The function was modified on the basis of previous studies (Hodos, 1961; Richardson and Roberts, 1996). Before the PR schedule, mice were tested in an FR10 session. For the optogenetic activation during PR, mice received 10 Hz photostimulation (10-ms pulses; 4-s laser on periods with 2-s laser off intervals; power, 10 mW; λ = 473 nm) during the entire PR session (60 min).

Optogenetic activation of aIC^{Fezf2}→NTS in differing behavioral contexts—The structure of the task in each session is similar to that of the reward-seeking task described above. In each trial of the task, a sound (CS, 1 s in duration) was presented, followed by a response window (1 s in duration). Licking during the response window led to distinct outcomes in different sessions. In each training session, water-restricted mice were trained to lick during the response window to obtain one of the following outcomes: water, 200 mM sucrose, 300 mM NaCl, or 5 mM quinine. Mice obtained 8 μl of the respective solution in each hit trial. In the test session, mice were first presented with 30 trials to remind them of the specific outcome, then tested with photoactivation of aIC^{Fezf2}→NTS pathway in 20% of randomly selected trials. The photoactivation was applied in the time window between CS onset and US onset (λ = 473 nm; power, 10 mW measured at the tip of optic fibers; 20 Hz with a 10-ms pulse width). For the extinction session, previously well-trained mice received extinction training in which licking during the response window no longer resulted in any outcome. For the quenched condition, well-trained mice were given free access to water before the test and then tested in a session where water was the outcome. For the test with Ensure (Ensure Original Nutrition Powder, Abbott), mice were food restricted to 85%

of free-feeding body weight, and then tested in a session where Ensure was the outcome (10 μl (0.015 calories) on each hit).

Real-time place preference/aversion (RTPP/A) test—Freely moving mice were initially habituated to a two-sided chamber (23 × 33 × 25 cm; made from Plexiglas) for 10 min, during which their baseline preference for the left or right side of the chamber was assessed. During the first test session (10 min), we assigned one side of the chamber (counterbalanced across mice) as the photostimulation side, and placed the mice in the non-stimulation side to start the experiment. Once the mouse entered the stimulation side, photostimulation, generated by a 473 nm laser (Shanghai Laser & Optics Century, Shanghai, China), was immediately turned on, and was turned off as soon as the mouse exited the stimulation side. In the second test session (10 min) we repeated this procedure but assigned the other side of the chamber as the stimulation side. For optogenetic activation, the photostimulation parameters were 10-ms pulse width, 20-Hz frequency, 10-mW power measured at fiber tips. For optogenetic inhibition, the photostimulation was 10-mW constant illumination. The mice were videotaped during the test with a CCD camera interfaced with Ethovision software (Noldus Information Technologies), which was also used to control the laser stimulation and extract behavioral parameters (position, time, distance and velocity).

Self-stimulation test—Freely moving mice were placed in a chamber equipped with two ports. Poking nose into one of the ports (the active port) triggered photostimulation (10-ms pulses, 20 Hz, 10 mW; λ = 473 nm) for 2 s in the NTS, whereas poking into the other port (the inactive port) did not trigger photostimulation. Mice were allowed to freely poke the two ports in 1-hour sessions, with the designation of active port in each session being counterbalanced.

Assessing food and liquid intake—Food or liquid intake was assessed in the home cage, where mice were individually housed. Mice were first food or water deprived for 24 hours. Their subsequent food or water intake in a 1-hour period was assessed. For optogenetic activation in this experiment, the photostimulation was 4-s trains of light pulses (10-ms pulse width, 20-Hz frequency, and 10-mW power measured at optical fiber tips) interleaved with 4-s light-off intervals. For optogenetic inhibition, the photostimulation was 4-s constant light illumination (10 mW) periods interleaved with 4-s light-off intervals. The light was generated by a 473 nm laser (Shanghai Laser & Optics Century, Shanghai, China). Experiments were conducted during the light-cycle, between 1 p.m. and 6 p.m.

To monitor liquid intake at a finer temporal resolution, we trained thirsty mice to obtain sucrose solution from a bottle in a chamber. These mice were subsequently tested in sessions containing laser-on and laser-off blocks. Each session contained 3 laser-off blocks and 3 laser-on blocks, with each block lasting 3 min. Each session started from either a laser-on or a laser-off block, with the two types of blocks interleaved with each other. For optogenetic activation in the light-on blocks, the photostimulation parameters were 10-ms pulse width, 20-Hz frequency, 10-mW power. For optogenetic inhibition in the light-on blocks, the photostimulation was constant light illumination (10-mW power). The light was generated by a 473 nm laser (Shanghai Laser & Optics Century, Shanghai, China).

Continuous licking task—Water deprived mice were trained to lick a spout to obtain a sucrose solution (200 mM). Each lick triggered the delivery of 0.3 μl of the solution. It took mice 4–7 days to achieve stable licking, the criterion of which was 10-min of continuous licking without any gap longer than 10 s. The mice were subsequently tested in the optogenetic manipulation experiments.

Behavioral data collection and analysis—Stimulus playback and trial control were performed via a Bpod/PulsePal open-source Arduino-based system (Sanworks, Stony Brook, NY, USA). Custom-written scripts in MATLAB based on Bpod commands were used to control the delivery of CS and US and record behavioral responses, including licking events, poking events and running velocity. Pure tones (70 dB; the CS) with different frequencies were generated as sine wave. The tones were uploaded to the audio adaptor board using the Bpod control system. The amount of liquid (the US) was controlled by fast solenoid valves (Lee Company). A metal spout was placed in front of the mouth of an animal for liquid delivery. In experiments which required delivery of sucrose and quinine, we used two tubes (one for each solution) epoxied together to avoid mixing of tastants. The spout also served as part of a custom “lickometer” circuit, which registered a lick event each time a mouse completed the circuit by licking the spout. The licking events were recorded and analyzed using custom scripts written in MATLAB. We used a rotary encoder (YUMO-E6B2-CWZ3E-1024; SparkFun Electronics) to detect and record real-time running velocity. The rotary encoder was attached to a running wheel and connected with a microcontroller (Arduino UNO R3; SparkFun Electronics). The running wheel (diameter, 14 cm; width, 8 cm) was made using a 3D printer (MakerBot Replicator 2; MakerBot). The microcontroller converted the digital inputs from the rotary encoder into analog signals reflecting running velocity, which was in turn recorded and analyzed with custom scripts written in MATLAB.

Calcium imaging and imaging data analysis—All imaging experiments were conducted on awake behaving mice under head-restraint in a dim, sound attenuated box. A one-photon imaging system modified from an Olympus BX51 microscope (Olympus Corporation, Shinjuku, Tokyo, Japan) with a 10 X objective (NA 0.3; Olympus, Cat. Number MPLFLN10x) was used to monitor GCaMP6 signals in behaving mice through the implanted GRIN lenses. The light source for imaging was a single-wavelength LED system (λ = 470 nm; http://www.coolled.com/) connected to the epifluorescence port of the Olympus BX51 microscope. The output power of the LED was set to 0.1–0.3 mW and was kept constant for the same subject across all imaging sessions. During imaging, the focus of the objective was adjusted such that the best dynamic fluorescence signals were at the focal plane. Visible landmarks, such as GCaMP6-expressing neurons and blood vessels, were used to help identify the same field of view (FOV) across different imaging sessions.

GCaMP6 fluorescence signals were captured with a monochrome CCD camera (pco.pixelfly, digital 14 bit CCD camera, image sensor ICX285AL) mounted onto the Olympus BX51. A custom Imaging Acquisition software written in LabVIEW (National Instruments) was used to interface the camera with a dedicated desktop computer and record the GCaMP6 signals at a frame rate of 10 frames/s. To synchronize imaging with behavioral events, Imaging Acquisition was triggered with a TTL (transistor-transistor logic) signal

from the Bpod State Machine (Sanworks) used for behavioral control. During imaging, the timestamps of different events, including the trigger signals sent to Imaging Acquisition, CS onset, US onset and licking events, were all recorded with Bpod.

For imaging data processing and analysis, we first used Inscopix Data Processing software (v.1.2.0., Inscopix) to spatially down-sample all the raw images by a factor of 4 to reduce file size, and to correct the image stack for motion artifacts. The motion-corrected images were cropped to remove post-registration borders and margin areas. The pre-processed image stack was exported as a .tif file. Next, we used the extended constrained non-negative matrix factorization optimized for one-photon imaging (CNMF-E) (Pnevmatikakis et al., 2016; Xiao et al., 2020; Zhang et al., 2021; Zhang and Li, 2018; Zhou et al., 2018) to demix neural signals and get their denoised and deconvolved temporal activity, termed ΔF (Pnevmatikakis et al., 2016; Zhou et al., 2018). We used the output C_raw, which corresponds to a scaled version of ΔF, for further analysis.

To determine whether a neuron was significantly ($P < 0.05$) excited or suppressed by a stimulus, and thus can be classified as being “responsive” to the stimulus, we used the Wilcoxon signed-rank test to compare the mean ΔF values in a period immediately after stimulus onset (the durations of which are indicated in figure legends) with those in the 4-s baseline period in all the trials imaged. For further analyses, such as the population analyses, we used z-scores to represent the dynamic activities in each neuron. To obtain the temporal z-scores for a neuron, we first obtained the mean activity trace for the neuron by averaging the fluorescence signals (ΔF) at each time point across all trials, and then computed the z-scores as $(F(t) - F_{mean})/F_{SD}$, where F(t) is the ΔF value at time t, F_{mean}, and F_{SD} are the mean and standard deviation, respectively, of the ΔF values over a 4-s baseline period.

To assess the temporal relationship between the onset of behavioral licking response and the onset of neuronal response, for each neuron, we calculated the z-scored neuronal activity at each time point and averaged the values across all trials; for the licking response, we calculated the licking rate at each time point (bin = 50 ms) and averaged the values across all trials. Next, we applied the change-point analysis (Gallistel et al., 2004; Paton et al., 2006) on these data to determine the time point at which the neuronal or behavioral response significantly changed (i.e., the change-point) following the presentation of CS. We repeated this for all neurons showing excitatory responses and calculated the difference between behavioral and neuronal change-points as the response delay for each neuron.

To analyze the trial-by-trial correlation between licking and neuronal responses, we first calculated the mean licking rate and the mean activity (z-scored) of each neuron during a specified time window (i.e., CS, US or baseline period) in each trial. We subsequently calculated the Pearson correlation coefficient between these two measures.

Evaluation of spatial clustering of neurons with specific functional properties—To test for spatial clustering of neurons with specific response properties at a relatively fine scale (tens of microns), we calculated pair-wise distances between all neurons. We then examined the distribution of distances between neurons that were either similar or different in their response type(s) (i.e., excited by sucrose vs. inhibited by sucrose).

Cell registration—To identify and track the same individual cells from images acquired in different imaging sessions, we performed cell registration as previously described (Sheintuch et al., 2017; Zhang et al., 2021; Zhang and Li, 2018). We used a probabilistic method which automatically registered cells across multiple imaging sessions and estimated the registration confidence for each registered cell. Briefly, we first used the CNMF-E analysis to generate the spatial footprints for all cells imaged in a reference session (e.g., sodium-depletion or early-learning session). We then repeated this process for the cells imaged in a target session (e.g., recovery from sodium-depletion or late-learning session). We used the footprints from the reference session as a reference map, and aligned with this map the footprints from the target session by correcting for translation and rotation differences between different sessions. We subsequently calculated the probability of a given pair of cells, each from one of the two imaging sessions, to be the same cell (P_{same}) based on their spatial correlation and centroid distance. A pair of cells is considered to have the same identity if $P_{same} > 0.95$. The centroid distance between a pair of cells deemed to have the same identity is generally small (≤ 6.5 μm).

Analysis of aIC^{Fezf2} population dynamics in the activity space—To assess the relationship between aIC^{Fezf2} population activity and different trial types in the go/no-go task, we used a previously described 'coding direction' analysis (Allen et al., 2019; Gao et al., 2018; Li et al., 2016; Xiao et al., 2020). For a population of n neurons, we found an $n \times 1$ vector in the n dimensional activity space that maximally separated the response vectors in two types of trials. We term this vector "coding direction (***cd***)". To obtain the ***cd*** of Hit and CR trials, for each neuron we first computed the average z-scored response in the two types of trials, r_{Hit} and r_{CR}, which are $n \times 1$ response vectors that describe the population response at each time point, t. We then computed the difference in the mean response vectors, $cd_t = r_{Hit} - r_{CR}$. We averaged the values of cd_t from CS onset to US onset to obtain a single ***cd***. For a population of n neurons, this yielded an $n \times 1$ vector. The projection of population activity in Hit and CR trials along the ***cd*** was obtained as $\boldsymbol{cd}^T r_{Hit}$ and $\boldsymbol{cd}^T r_{CR}$, respectively.

Population vector analysis—To quantify learning-induced changes in the similarity between neuronal responses at population level, we performed population vector analysis as previously described (Rozeske et al., 2018; Zhang and Li, 2018). Briefly, we created a series of n-dimensional (n = number of neurons) activity vectors for the responses (z-scored) of individual neurons at each time point. Therefore, the ensemble neuronal response at a particular time point is represented by a vector with a dimension equal to the total number of neurons in that ensemble. We computed the Mahalanobis distance (MD) between the vectors as a measure of the similarity between ensemble neuronal representations. For example, the MD between the ensemble representations to CS and US in hit trials in the go/no-go task is defined as:

$$MD(CS_{Hit}, US_{Hit}) = \sqrt{(PV(CS_{Hit}) - PV(US_{Hit}))^T * S^{-1}(PV(CS_{Hit}) - PV(US_{Hit}))}$$

where $PV(CS_{Hit})$ and $PV(US_{Hit})$ are the individual and mean population vectors of responses to CS and US, respectively, in hit trials. S^{-1} is the inverse of the covariance matrix. The responses in a 3-s time window immediately after CS or US onset in the hit

trials of the go/no-go task was used to generate the population vectors. The MD takes into account the differences in the means of the two sets of ensemble responses as well as their covariances.

For data visualization purpose, we used principal component analysis (PCA) for dimensionality reduction, and projected the population vectors onto a two-dimensional space.

Decoding analysis—We performed population decoding analysis using the linear support vector machine (SVM) in MATLAB (fitcsvm) to determine whether the types of trials could be predicted on the basis of the trial-by-trial population activities of aIC^{Fezf2} or aIC^{NTS} neurons acquired in each session. We used the activities of all the simultaneously imaged neurons in each session to perform the population decoding analysis. To compare decoding accuracy between aIC^{Fezf2} and aIC^{NTS} neurons, we pooled all the aIC^{Fezf2} or aIC^{NTS} neurons and randomly sampled a certain number of neurons from each population to perform the population analysis (iteration: 100 times). First, we applied principal component analysis (PCA) on the matrix of z-scored trial-by-trial neuronal activities. We used the first two or three PCs to represent the population activity in each trial. We subsequently used a subset of the low dimensional trial-by-trial neuronal activity data as the training dataset to train a classifier with linear kernel function ('linear') for two-class decoding (e.g., classifying large-reward block and small-reward block). Finally, we validated the classifier by using the 'predict' function to classify the trial-by-trial neuronal activities in the test dataset. Activities from randomly selected 75% of trials of each type were used to train the classifier, and activities from the remaining 25% of trials of each type were used to test decoding accuracy. To generate the shuffled data, we randomly reassigned a trial type to each of the trial-by-trial neuronal activities. We then followed the same procedure as that used for classifying the actual data to decode the shuffled data. We repeated this classification process 1,000 times for both the actual test dataset and the shuffled data, and calculated the average accuracy as the decoding accuracy.

***In vivo* fiber photometry and data analysis—**To record the activities of $NTS^{Recipient}$ neurons or dopamine release in nucleus accumbens *in vivo* in behaving animals, we used a commercial fiber photometry system (Neurophotometrics Ltd., San Diego, CA, USA) to measure GCaMP6 or DA2m signals through an optical fiber implanted in the NTS or NAc core. A patch cord (fiber core diameter, 200 μm; Doric Lenses) was used to connect the photometry system with the implanted optical fiber. The intensity of the blue light (λ = 470 nm) for excitation was adjusted to a low level (20~50 μW) at the tip of the patch cord. Emitted fluorescence was bandpass filtered and focused onto the sensor of a CCD camera. Photometry signals and behavioral events were aligned based on an analog TTL signal generated by the Bpod. Mean values of signals from a region of interest were calculated and saved by using Bonsai software (Bonsai), and were exported to MATLAB for further analysis.

To correct for photobleaching of fluorescence signals (baseline drift), a bi-exponential curve was fit to the raw fluorescence trace and subtracted as follows:

$$F_{raw\_fit} = fit(Timestamp, F_{raw}, 'exp2')$$

$$F_{raw\_correction} = \frac{F_{raw} - F_{raw\_fit}}{F_{raw\_fit}}$$

After baseline drift correction, the fluorescence signals were z-scored relative to the mean and standard deviation of the signals in a time window −4 to 0 s relative to CS onset.

For the simultaneous optogenetic stimulation and photometry experiments, the mice received photostimulation in the NTS in the window between CS onset and US onset (3-s duration) in 33% of randomly selected trials, while we recorded DA2m fluorescence signals in NAc core using fiber photometry. The photostimulation parameters were 20-Hz pulse frequency, 10-ms pulse width, 5-mW power, 473-nm wavelength.

To identify pairs of laser-off and laser-on go trials with comparable lick rates, we first calculated the average lick rate from CS onset to US onset for each trial. We then searched all the laser-off trials for trials having the lick rates within 10% ± the rate of a laser-on trial. Of these, we then selected the laser-off trial that had a lick rate nearest to that of the laser-on trial. We compared the DA2m signals in such “matched” laser-off and laser-on trials. We used a lower power of laser for the stimulation to minimize the effect on licking, and thus increase the number of laser-on trials with lick rates comparable to those in laser-off trials.

QUANTIFICATION AND STATISTICAL ANALYSIS

Statistical analyses were performed using Matlab or a commercial software (GraphPad Prism; GraphPad Software, CA). The statistical test used for each comparison is indicated when used. Analysis of variance (ANOVA) was used to check for main effects and interactions in experiments with repeated measures and more than one factor. When main effects or interactions were significant, we did the planned comparisons according to experimental design (for example, comparing laser on and off conditions). All comparisons were two tailed. Threshold for significance was placed at *p<0.05, **p<0.01, ***p<0.001 and ****p<0.0001. The box-and-whisker plots indicate median, first and third quartiles, and min and max values. All data are shown as mean ± standard error of the mean (SEM) unless stated otherwise.

Supplementary Material

Refer to Web version on PubMed Central for supplementary material.

ACKNOWLEDGEMENTS

We thank Dr. Alfredo Fontanini (Stony Brook University) and Dr. Tianyi Mao (Vollum Institute, Oregon Health & Science University) for comments on an earlier version of the manuscript, Dr. Pengcheng Zhou (Columbia University and Shenzhen Institutes of Advanced Technology, Chinese Academy of Sciences) for advice and the MATLAB code for CNMF-E analysis, Taylor Russo and Radhashree Sharma for technical assistance, and members of the Li laboratory for helpful discussions. This work was supported by grants from National Institutes of Health

(NIH) (R01MH101214, R01MH108924, R01DA050374, R01NS104944, B.L.), the Cold Spring Harbor Laboratory and Northwell Health Affiliation (B.L.), and Feil Family Neuroscience Endowment (B.L.).

REFERENCES

Allen WE, Chen MZ, Pichamoorthy N, Tien RH, Pachitariu M, Luo L, and Deisseroth K (2019). Thirst regulates motivated behavior through modulation of brainwide neural population dynamics. Science 364.

Baldo BA, and Kelley AE (2007). Discrete neurochemical coding of distinguishable motivational processes: insights from nucleus accumbens control of feeding. Psychopharmacology (Berl) 191, 439–459. [PubMed: 17318502]

Berditchevskaia A, Caze RD, and Schultz SR (2016). Performance in a GO/NOGO perceptual task reflects a balance between impulsive and instrumental components of behaviour. Sci Rep 6, 27389. [PubMed: 27272438]

Berke JD (2018). What does dopamine mean? Nat Neurosci 21, 787–793. [PubMed: 29760524]

Berridge KC, Robinson TE, and Aldridge JW (2009). Dissecting components of reward: 'liking', 'wanting', and learning. Curr Opin Pharmacol 9, 65–73. [PubMed: 19162544]

Bonson KR, Grant SJ, Contoreggi CS, Links JM, Metcalfe J, Weyl HL, Kurian V, Ernst M, and London ED (2002). Neural systems and cue-induced cocaine craving. Neuropsychopharmacology 26, 376–386. [PubMed: 11850152]

Chen K, Kogan JF, and Fontanini A (2020). Spatially Distributed Representation of Taste Quality in the Gustatory Insular Cortex of Behaving Mice. Curr Biol 31 247–256.e244. [PubMed: 33186554]

Chen TW, Wardill TJ, Sun Y, Pulver SR, Renninger SL, Baohan A, Schreiter ER, Kerr RA, Orger MB, Jayaraman V, et al. (2013). Ultrasensitive fluorescent proteins for imaging neuronal activity. Nature 499, 295–300. [PubMed: 23868258]

Chen X, Gabitto M, Peng Y, Ryba NJ, and Zuker CS (2011). A gustotopic map of taste qualities in the mammalian brain. Science 333, 1262–1266. [PubMed: 21885776]

Chen X, Sun YC, Zhan H, Kebschull JM, Fischer S, Matho K, Huang ZJ, Gillis J, and Zador AM (2019). High-Throughput Mapping of Long-Range Neuronal Projection Using In Situ Sequencing. Cell 179, 772–786 e719. [PubMed: 31626774]

Contreras M, Ceric F, and Torrealba F (2007). Inactivation of the interoceptive insula disrupts drug craving and malaise induced by lithium. Science 318, 655–658. [PubMed: 17962567]

Craig AD (2009). How do you feel--now? The anterior insula and human awareness. Nat Rev Neurosci 10, 59–70. [PubMed: 19096369]

Critchley HD, and Harrison NA (2013). Visceral influences on brain and behavior. Neuron 77, 624–638. [PubMed: 23439117]

Dikecligil GN, Graham DM, Park IM, and Fontanini A (2020). Layer- and Cell Type-Specific Response Properties of Gustatory Cortex Neurons in Awake Mice. J Neurosci 40, 9676–9691. [PubMed: 33172981]

du Hoffmann J, and Nicola SM (2014). Dopamine invigorates reward seeking by promoting cue-evoked excitation in the nucleus accumbens. J Neurosci 34, 14349–14364. [PubMed: 25339748]

Emiliani V, Cohen AE, Deisseroth K, and Hausser M (2015). All-Optical Interrogation of Neural Circuits. J Neurosci 35, 13917–13926. [PubMed: 26468193]

Engelmann JM, Versace F, Robinson JD, Minnix JA, Lam CY, Cui Y, Brown VL, and Cinciripini PM (2012). Neural substrates of smoking cue reactivity: a meta-analysis of fMRI studies. Neuroimage 60, 252–262. [PubMed: 22206965]

Etkin A (2010). Functional neuroanatomy of anxiety: a neural circuit perspective. Curr Top Behav Neurosci 2, 251–277. [PubMed: 21309113]

Fenno LE, Mattis J, Ramakrishnan C, Hyun M, Lee SY, He M, Tucciarone J, Selimbeyoglu A, Berndt A, Grosenick L, et al. (2014). Targeting cells with single vectors using multiple-feature Boolean logic. Nat Methods 11, 763–772. [PubMed: 24908100]

Floresco SB (2015). The nucleus accumbens: an interface between cognition, emotion, and action. Annu Rev Psychol 66, 25–52. [PubMed: 25251489]

Forget B, Pushparaj A, and Le Foll B (2010). Granular Insular Cortex Inactivation as a Novel Therapeutic Strategy for Nicotine Addiction. Biological Psychiatry 68, 265–271. [PubMed: 20299008]

Fu Y, Yuan Y, Halliday G, Rusznak Z, Watson C, and Paxinos G (2012). A cytoarchitectonic and chemoarchitectonic analysis of the dopamine cell groups in the substantia nigra, ventral tegmental area, and retrorubral field in the mouse. Brain Struct Funct 217, 591–612. [PubMed: 21935672]

Gallistel CR, Fairhurst S, and Balsam P (2004). The learning curve: implications of a quantitative analysis. Proc Natl Acad Sci U S A 101, 13124–13131. [PubMed: 15331782]

Gao Z, Davis C, Thomas AM, Economo MN, Abrego AM, Svoboda K, De Zeeuw CI, and Li N (2018). A cortico-cerebellar loop for motor planning. Nature 563, 113–116. [PubMed: 30333626]

Gogolla N (2017). The insular cortex. Curr Biol 27, R580–R586. [PubMed: 28633023]

Govorunova EG, Sineshchekov OA, Janz R, Liu X, and Spudich JL (2015). Natural light-gated anion channels: A family of microbial rhodopsins for advanced optogenetics. Science 349, 647–650. [PubMed: 26113638]

Hamid AA, Pettibone JR, Mabrouk OS, Hetrick VL, Schmidt R, Vander Weele CM, Kennedy RT, Aragona BJ, and Berke JD (2016). Mesolimbic dopamine signals the value of work. Nat Neurosci 19, 117–126. [PubMed: 26595651]

Harris KD, and Mrsic-Flogel TD (2013). Cortical connectivity and sensory coding. Nature 503, 51–58. [PubMed: 24201278]

Harris KD, and Shepherd GM (2015). The neocortical circuit: themes and variations. Nat Neurosci 18, 170–181. [PubMed: 25622573]

He M, Liu Y, Wang X, Zhang MQ, Hannon GJ, and Huang ZJ (2012). Cell-type-based analysis of microRNA profiles in the mouse brain. Neuron 73, 35–48. [PubMed: 22243745]

Hodos W (1961). Progressive ratio as a measure of reward strength. Science 134, 943–944. [PubMed: 13714876]

Jin H, Fishman ZH, Ye MY, Wang L, and Zuker CS (2021). Top-Down Control of Sweet and Bitter Taste in the Mammalian Brain. Cell 184, 257–271.e216. [PubMed: 33417862]

Katz DB, Simon SA, and Nicolelis MA (2001). Dynamic and multimodal responses of gustatory cortical neurons in awake rats. J Neurosci 21, 4478–4489. [PubMed: 11404435]

Ko D, and Wanat MJ (2016). Phasic Dopamine Transmission Reflects Initiation Vigor and Exerted Effort in an Action- and Region-Specific Manner. J Neurosci 36, 2202–2211. [PubMed: 26888930]

Kuhn S, and Gallinat J (2011). Common biology of craving across legal and illegal drugs - a quantitative meta-analysis of cue-reactivity brain response. Eur J Neurosci 33, 1318–1326. [PubMed: 21261758]

Kusumoto-Yoshida I, Liu H, Chen BT, Fontanini A, and Bonci A (2015). Central role for the insular cortex in mediating conditioned responses to anticipatory cues. Proc Natl Acad Sci U S A 112, 1190–1195. [PubMed: 25583486]

Lee S, Augustine V, Zhao Y, Ebisu H, Ho B, Kong D, and Oka Y (2019). Chemosensory modulation of neural circuits for sodium appetite. Nature 568, 93–97. [PubMed: 30918407]

Lee W, and Reeve J (2013). Self-determined, but not non-self-determined, motivation predicts activations in the anterior insular cortex: an fMRI study of personal agency. Soc Cogn Affect Neurosci 8, 538–545. [PubMed: 22451482]

Lee W, and Reeve J (2017). Identifying the neural substrates of intrinsic motivation during task performance. Cogn Affect Behav Neurosci 17, 939–953. [PubMed: 28639132]

Li N, Daie K, Svoboda K, and Druckmann S (2016). Robust neuronal dynamics in premotor cortex during motor planning. Nature 532, 459–464. [PubMed: 27074502]

Livneh Y, Ramesh RN, Burgess CR, Levandowski KM, Madara JC, Fenselau H, Goldey GJ, Diaz VE, Jikomes N, Resch JM, et al. (2017). Homeostatic circuits selectively gate food cue responses in insular cortex. Nature 546, 611–616. [PubMed: 28614299]

Livneh Y, Sugden AU, Madara JC, Essner RA, Flores VI, Sugden LA, Resch JM, Lowell BB, and Andermann ML (2020). Estimation of Current and Future Physiological States in Insular Cortex. Neuron 105, 1094–1111 e1010. [PubMed: 31955944]

Lodato S, Molyneaux BJ, Zuccaro E, Goff LA, Chen HH, Yuan W, Meleski A, Takahashi E, Mahony S, Rinn JL, et al. (2014). Gene co-regulation by Fezf2 selects neurotransmitter identity and connectivity of corticospinal neurons. Nat Neurosci 17, 1046–1054. [PubMed: 24997765]

Luijten M, Veltman DJ, van den Brink W, Hester R, Field M, Smits M, and Franken IH (2011). Neurobiological substrate of smoking-related attentional bias. Neuroimage 54, 2374–2381. [PubMed: 20932921]

Maffei A, Haley M, and Fontanini A (2012). Neural processing of gustatory information in insular circuits. Curr Opin Neurobiol 22, 709–716. [PubMed: 22554880]

Mahn M, Gibor L, Patil P, Cohen-Kashi Malina K, Oring S, Printz Y, Levy R, Lampl I, and Yizhar O (2018). High-efficiency optogenetic silencing with soma-targeted anion-conducting channelrhodopsins. Nat Commun 9, 4125. [PubMed: 30297821]

Manes F, Paradiso S, and Robinson RG (1999). Neuropsychiatric effects of insular stroke. Journal of Nervous and Mental Disease 187, 707–712. [PubMed: 10665464]

Matho KS, Huilgol D, Galbavy W, He M, Kim G, An X, Lu J, Wu P, Di Bella DJ, Shetty AS, et al. (2021). Genetic dissection of the glutamatergic neuron system in cerebral cortex. Nature 598, 182–187. [PubMed: 34616069]

Menon V, and Uddin LQ (2010). Saliency, switching, attention and control: a network model of insula function. Brain Struct Funct 214, 655–667. [PubMed: 20512370]

Mohebi A, Pettibone JR, Hamid AA, Wong JT, Vinson LT, Patriarchi T, Tian L, Kennedy RT, and Berke JD (2019). Dissociable dopamine dynamics for learning and motivation. Nature 570, 65–70. [PubMed: 31118513]

Mutschler I, Hänggi J, Frei M, Lieb R, grosse Holforth M, Seifritz E, and Spinelli S (2019). Insular volume reductions in patients with major depressive disorder. Neurology, psychiatry and brain research 33, 39–47.

Naqvi NH, Gaznick N, Tranel D, and Bechara A (2014). The insula: a critical neural substrate for craving and drug seeking under conflict and risk. Ann N Y Acad Sci 1316, 53–70. [PubMed: 24690001]

Naqvi NH, Rudrauf D, Damasio H, and Bechara A (2007). Damage to the insula disrupts addiction to cigarette smoking. Science 315, 531–534. [PubMed: 17255515]

Niv Y, Daw ND, Joel D, and Dayan P (2007). Tonic dopamine: opportunity costs and the control of response vigor. Psychopharmacology (Berl) 191, 507–520. [PubMed: 17031711]

Paton JJ, Belova MA, Morrison SE, and Salzman CD (2006). The primate amygdala represents the positive and negative value of visual stimuli during learning. Nature 439, 865–870. [PubMed: 16482160]

Paulus MP, and Stein MB (2010). Interoception in anxiety and depression. Brain Struct Funct 214, 451–463. [PubMed: 20490545]

Peng Y, Gillis-Smith S, Jin H, Trankner D, Ryba NJ, and Zuker CS (2015). Sweet and bitter taste in the brain of awake behaving animals. Nature 527, 512–515. [PubMed: 26580015]

Pnevmatikakis EA, Soudry D, Gao Y, Machado TA, Merel J, Pfau D, Reardon T, Mu Y, Lacefield C, Yang W, et al. (2016). Simultaneous Denoising, Deconvolution, and Demixing of Calcium Imaging Data. Neuron 89, 285–299. [PubMed: 26774160]

Quadt L, Critchley HD, and Garfinkel SN (2018). The neurobiology of interoception in health and disease. Ann N Y Acad Sci 1428, 112–128. [PubMed: 29974959]

Reardon TR, Murray AJ, Turi GF, Wirblich C, Croce KR, Schnell MJ, Jessell TM, and Losonczy A (2016). Rabies Virus CVS-N2c(DeltaG) Strain Enhances Retrograde Synaptic Transfer and Neuronal Viability. Neuron 89, 711–724. [PubMed: 26804990]

Richardson NR, and Roberts DC (1996). Progressive ratio schedules in drug self-administration studies in rats: a method to evaluate reinforcing efficacy. J Neurosci Methods 66, 1–11. [PubMed: 8794935]

Rigoli F, Chew B, Dayan P, and Dolan RJ (2016). The Dopaminergic Midbrain Mediates an Effect of Average Reward on Pavlovian Vigor. J Cogn Neurosci 28, 1303–1317. [PubMed: 27082045]

Rozeske RR, Jercog D, Karalis N, Chaudun F, Khoder S, Girard D, Winke N, and Herry C (2018). Prefrontal-Periaqueductal Gray-Projecting Neurons Mediate Context Fear Discrimination. Neuron 97, 898–910 e896. [PubMed: 29398355]

Salamone JD, Correa M, Yang JH, Rotolo R, and Presby R (2018). Dopamine, Effort-Based Choice, and Behavioral Economics: Basic and Translational Research. Front Behav Neurosci 12, 52. [PubMed: 29628879]

Samuelsen CL, and Fontanini A (2017). Processing of Intraoral Olfactory and Gustatory Signals in the Gustatory Cortex of Awake Rats. Journal of Neuroscience 37, 244–257. [PubMed: 28077705]

Samuelsen CL, Gardner MPH, and Fontanini A (2012). Effects of Cue-Triggered Expectation on Cortical Processing of Taste. Neuron 74, 410–422. [PubMed: 22542192]

Sheintuch L, Rubin A, Brande-Eilat N, Geva N, Sadeh N, Pinchasof O, and Ziv Y (2017). Tracking the Same Neurons across Multiple Days in Ca(2+) Imaging Data. Cell Rep 21, 1102–1115. [PubMed: 29069591]

Shipley MT (1982). Insular cortex projection to the nucleus of the solitary tract and brainstem visceromotor regions in the mouse. Brain Res Bull 8, 139–148. [PubMed: 7066705]

Shuvaev SA, Tran NB, Stephenson-Jones M, Li B, and Koulakov AA (2020). Neural Networks With Motivation. Front Syst Neurosci 14, 609316. [PubMed: 33536879]

Sliz D, and Hayley S (2012). Major depressive disorder and alterations in insular cortical activity: a review of current functional magnetic imaging research. Front Hum Neurosci 6, 323. [PubMed: 23227005]

Sprengelmeyer R, Steele JD, Mwangi B, Kumar P, Christmas D, Milders M, and Matthews K (2011). The insular cortex and the neuroanatomy of major depression. J Affect Disord 133, 120–127. [PubMed: 21531027]

Stephenson-Jones M, Bravo-Rivera C, Ahrens S, Furlan A, Xiao X, Fernandes-Henriques C, and Li B (2020). Opposing Contributions of GABAergic and Glutamatergic Ventral Pallidal Neurons to Motivational Behaviors. Neuron 105, 921–933 e925. [PubMed: 31948733]

Stratmann M, Konrad C, Kugel H, Krug A, Schoning S, Ohrmann P, Uhlmann C, Postert C, Suslow T, Heindel W, et al. (2014). Insular and hippocampal gray matter volume reductions in patients with major depressive disorder. PLoS One 9, e102692. [PubMed: 25051163]

Sun F, Zeng J, Jing M, Zhou J, Feng J, Owen SF, Luo Y, Li F, Wang H, Yamaguchi T, et al. (2018). A Genetically Encoded Fluorescent Sensor Enables Rapid and Specific Detection of Dopamine in Flies, Fish, and Mice. Cell 174, 481–496 e419. [PubMed: 30007419]

Sun F, Zhou J, Dai B, Qian T, Zeng J, Li X, Zhuo Y, Zhang Y, Wang Y, Qian C, et al. (2020). Next-generation GRAB sensors for monitoring dopaminergic activity in vivo. Nat Methods 17, 1156–1166. [PubMed: 33087905]

Suter BA, Migliore M, and Shepherd GM (2013). Intrinsic electrophysiology of mouse corticospinal neurons: a class-specific triad of spike-related properties. Cereb Cortex 23, 1965–1977. [PubMed: 22761308]

Tasic B, Yao Z, Graybuck LT, Smith KA, Nguyen TN, Bertagnolli D, Goldy J, Garren E, Economo MN, Viswanathan S, et al. (2018). Shared and distinct transcriptomic cell types across neocortical areas. Nature 563, 72–78. [PubMed: 30382198]

Tindell AJ, Smith KS, Berridge KC, and Aldridge JW (2009). Dynamic computation of incentive salience: “wanting” what was never “liked”. J Neurosci 29, 12220–12228. [PubMed: 19793980]

Venniro M, Caprioli D, Zhang M, Whitaker LR, Zhang S, Warren BL, Cifani C, Marchant NJ, Yizhar O, Bossert JM, et al. (2017). The Anterior Insular Cortex-->Central Amygdala Glutamatergic Pathway Is Critical to Relapse after Contingency Management. Neuron 96, 414–427 e418. [PubMed: 29024664]

Vincis R, and Fontanini A (2016). A gustocentric perspective to understanding primary sensory cortices. Current Opinion in Neurobiology 40, 118–124. [PubMed: 27455038]

Wang L, Gillis-Smith S, Peng Y, Zhang J, Chen X, Salzman CD, Ryba NJP, and Zuker CS (2018). The coding of valence and identity in the mammalian taste system. Nature 558, 127–131. [PubMed: 29849148]

Wu Y, Chen C, Chen M, Qian K, Lv X, Wang H, Jiang L, Yu L, Zhuo M, and Qiu S (2020). The anterior insular cortex unilaterally controls feeding in response to aversive visceral stimuli in mice. Nat Commun 11, 640. [PubMed: 32005806]

Xiao X, Deng H, Furlan A, Yang T, Zhang X, Hwang GR, Tucciarone J, Wu P, He M, Palaniswamy R, et al. (2020). A Genetically Defined Compartmentalized Striatal Direct Pathway for Negative Reinforcement. Cell 183, 211–227 e220. [PubMed: 32937106]

Yao Z, van Velthoven CTJ, Nguyen TN, Goldy J, Sedeno-Cortes AE, Baftizadeh F, Bertagnolli D, Casper T, Chiang M, Crichton K, et al. (2021). A taxonomy of transcriptomic cell types across the isocortex and hippocampal formation. Cell 184, 3222–3241 e3226. [PubMed: 34004146]

Zhang X, Guan W, Yang T, Furlan A, Xiao X, Yu K, An X, Galbavy W, Ramakrishnan C, Deisseroth K, et al. (2021). Genetically identified amygdala-striatal circuits for valence-specific behaviors. Nat Neurosci 24, 1586–1600. [PubMed: 34663958]

Zhang X, and Li B (2018). Population coding of valence in the basolateral amygdala. Nat Commun 9, 5195. [PubMed: 30518754]

Zhou P, Resendez SL, Rodriguez-Romaguera J, Jimenez JC, Neufeld SQ, Giovannucci A, Friedrich J, Pnevmatikakis EA, Stuber GD, Hen R, et al. (2018). Efficient and accurate extraction of in vivo calcium signals from microendoscopic video data. Elife 7.

Zingg B, Chou XL, Zhang ZG, Mesik L, Liang F, Tao HW, and Zhang LI (2017). AAV-Mediated Anterograde Transsynaptic Tagging: Mapping Corticocollicular Input-Defined Neural Pathways for Defense Behaviors. Neuron 93, 33–47. [PubMed: 27989459]

Highlights

- Neurons in the aIC^{Fezf2}→NTS circuit acquire anticipatory activity through learning
- The anticipatory activity encodes the perceived value and motivation
- aIC^{Fezf2}→NTS controls vigor, effort and striatal dopamine release
- aIC^{Fezf2}→NTS function depends on both learning and homeostatic demand

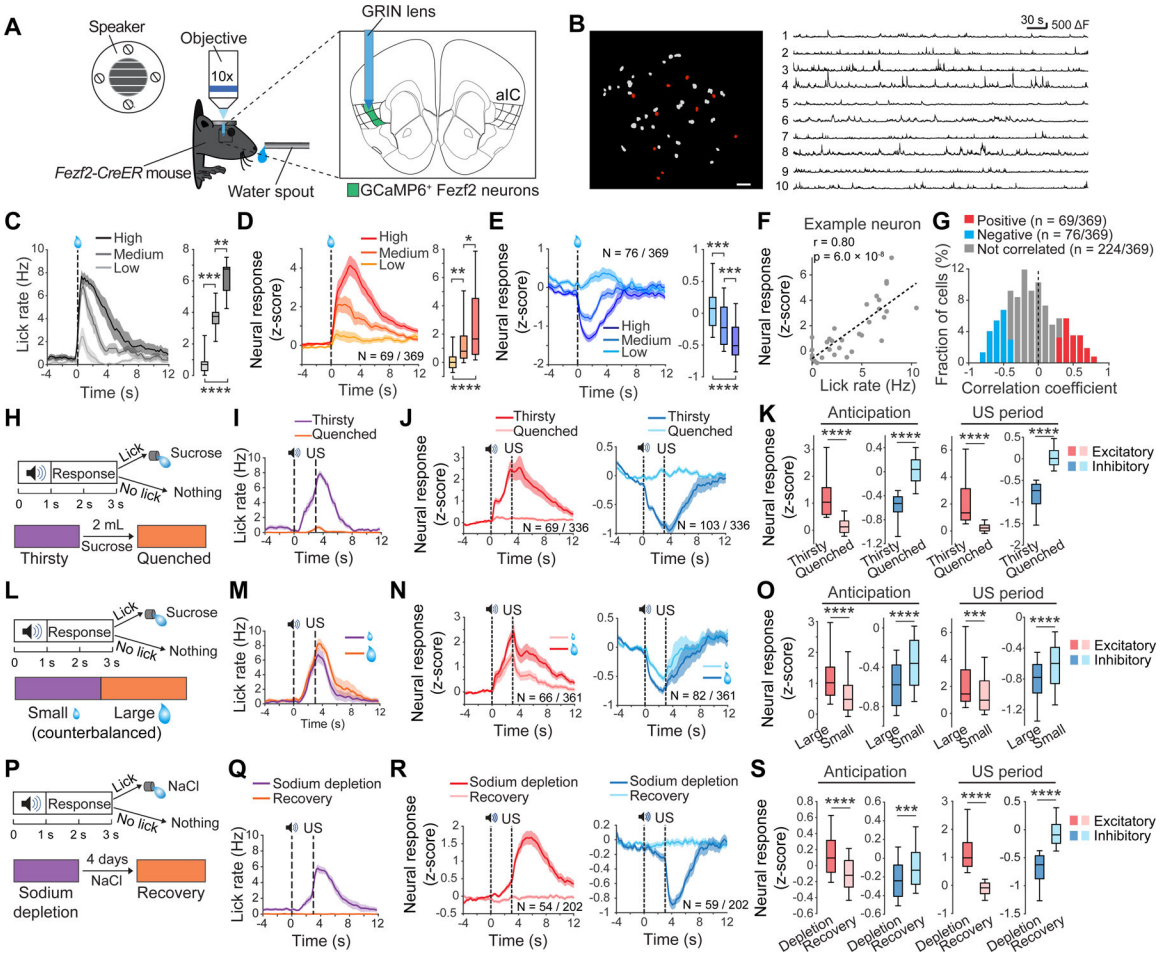

Figure 1. aIC^{Fezf2} neuron activity is modulated by action vigor and motivational state

(A) Schematics of the setup (left) and location in the aIC (right) for imaging.

(B) Left, the spatial locations of individual extracted neurons. In red are 10 example neurons whose activity traces are shown in the right.

(C) Left, average licking rates in different trial types. Right, quantification of average licking rates during the 4-s period following tastant delivery ($F_{(2,15)}$ = 38.79, P < 0.0001; **P = 0.0022, ***P = 0.0009, ****P < 0.0001; one-way ANOVA followed by Tukey's test).

(D) (CLeft, average responses of the neurons showing significant positive correlations in (G) in different trial types. Right, quantification of average responses during the 4-s period following tastant delivery ($F_{(2,204)}$ = 17.32, P < 0.0001; *P = 0.014, **P = 0.0073, ****P < 0.0001; one-way ANOVA followed by Tukey's test).

(E) Same as (D), except that the neurons are those showing significant negative correlations in (G) ($F_{(2,225)}$ = 32.35, P < 0.0001; ***P = 0.0001 (low vs. medium), ***P = 0.0004 (medium vs. high), ****P < 0.0001; one-way ANOVA followed by Tukey's test).

(F) An example neuron showing a positive correlation between its responses and licking rates following US delivery (Pearson's r = 0.80, P < 0.0001). Each dot represents one trial.

(G) Distribution of all the neurons' Pearson's correlation coefficients calculated as in (F). Red, blue and gray bars represent neurons showing significant positive (P < 0.05), significant negative (P < 0.05) and non-significant (P > 0.05) correlations, respectively.

(H) A schematic of the task.

(I) Average licking rates of a mouse in thirsty and quenched states.

(J) Average activity traces of neurons showing excitatory (left) or inhibitory (right) response under thirsty and quenched states.

(K) Quantification of the average responses shown in (J), during the anticipation (0–3 s; left) and US (3–5 s; right) periods (****P < 0.0001, Wilcoxon signed-rank test).

(L) A schematic of the task.

(M) Average licking rates of a mouse in the small- and large-reward blocks.

(N) Average activity traces of neurons showing excitatory (left) or inhibitory (right) response to the presentation of US in the large- and small-reward blocks.

(O) Quantification of the average responses shown in (N), during the anticipation (0–3 s; left) and US (3–5 s; right) periods (*** P < 0.001, ****P < 0.0001, Wilcoxon signed-rank test).

(P) A schematic of the task.

(Q) Average licking rates of a mouse under sodium-depletion and after recovery.

(R) Average activity traces of neurons showing excitatory (left) or inhibitory (right) response to the presentation of US in mice under sodium depletion and after recovery.

(S) Quantification of the average responses shown in (R), during the anticipation (0–3 s; left) and US (3–5 s; right) periods (***P < 0.001, ****P < 0.0001, Wilcoxon signed-rank test).

Data are presented as mean ± s.e.m. or box-and-whisker plots. See also Figure S1, S2, and Video S1.

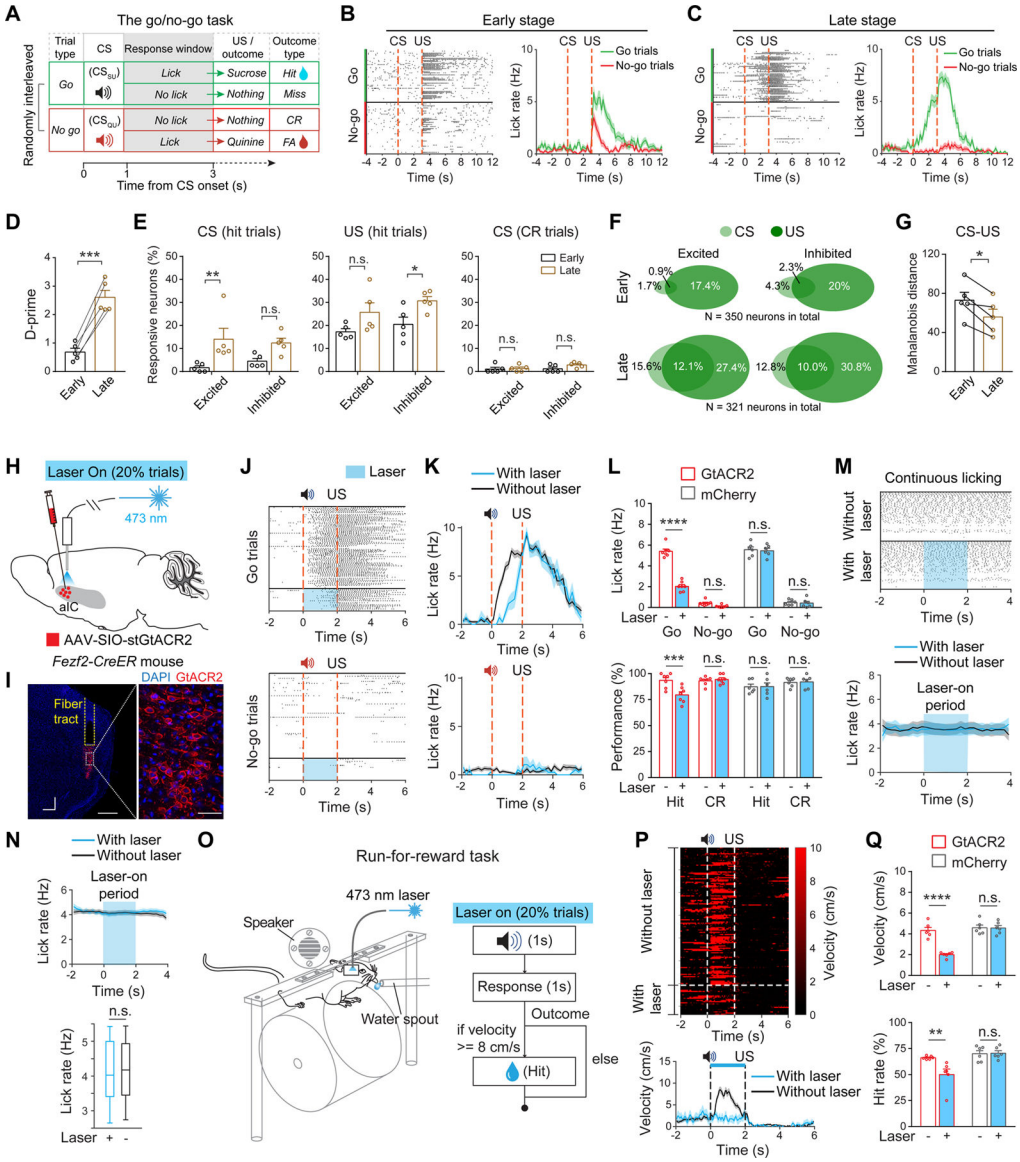

Figure 2. Learning induces anticipatory signals essential for motivational actions

(A) A schematic of the task design. CR, correct rejection; FA, false alarm.

(B, C) Licking events (left) and average licking rates (right) from a mouse at the early (B) and late (C) stages of training.

(D) D-prime at different stages of training ($t_{(4)}$ = 9.84, ***P = 0.0006, paired t-test).

(E) Percentage of aIC^{Fezf2} neurons showing responses at different stages of training. Left, CS responses in hit trials ($F_{(1,16)}$ = 14.3, P = 0.0016; excited neurons, **P = 0.0098; inhibited neurons, P = 0.11). Middle, US responses in hit trials ($F_{(1,16)}$ = 10.85, P = 0.0046; excited neurons, P = 0.10; inhibited neurons, *P = 0.043). Right, CS responses in CR trials ($F_{(1,16)}$ = 1.05, P = 0.32; excited neurons, n.s., P > 0.99; inhibited neurons, n.s., P = 0.21). Two-way ANOVA followed by Bonferroni's test.

(F) Percentage distributions of the neurons excited (left) and inhibited (right) by CS and US in hit trials at the early (top) and late (bottom) stages of training.

(G) Mahalanobis distance between vectors representing CS and US responses in hit trials at different stages of training ($t_{(4)}$ = 4.06, *P = 0.015, paired t-test).
(H) A schematic of the approach.
(I) Confocal images showing the expression of GtACR2 in aIC^{Fezf2} neurons and optic fiber placement. On the right is a high-magnification image of the boxed area on the left.
(J, K) Licking rasters (J) and average licking rates (K) of a GtACR2 mouse in one session. Top, go trials; bottom, no-go trials. Blue rectangles indicate the window of laser stimulation.
(L) Top, lick rate during anticipation period (0–2 s) (GtACR2: n = 7 mice, $F_{(1,12)}$ = 165.9, P < 0.0001; go trials, ****P < 0.0001; no-go trials, n.s., P = 0.20; mCherry: n = 6 mice, $F_{(1,10)}$ = 0.011, P = 0.92; go and no-go trials, n.s., P > 0.99). Bottom, performance (GtACR2: $F_{(1,12)}$ = 20.19, P = 0.0007; hit, ***P = 0.0002; CR, n.s., P > 0.99; mCherry: $F_{(1,10)}$ = 0.012, P = 0.92; hit and CR, P > 0.99). Two-way ANOVA followed by Bonferroni's test.
(M) Licking behavior of a GtACR2 mouse in the continuous licking task. Top, licking rasters; bottom, average licking rates.
(N) Quantification of licking behavior in the continuous licking task. Top, average licking rate across mice; bottom, average licking rate during the 0–2 s window (n = 7 mice; P = 0.59, Wilcoxon signed-rank test).
(O) Schematics of task setup (left) and design (right).
(P) Running behavior of a GtACR2 mouse in one session. Top, trial-by-trial velocity heatmap sorted according to trial types. Bottom, average running velocity; blue bar indicates the window of laser stimulation.
(**Q**) Top, running velocity during anticipation period (0–2 s) ($F_{(1,10)}$ = 59.95, P < 0.0001; GtACR2, n = 6, ****P < 0.0001; mCherry, n = 6, n.s., P > 0.99). Bottom, hit rate ($F_{(1,10)}$ = 8.69, P = 0.015; GtACR2, **P = 0.0048; mCherry, n.s., P > 0.99). Two-way ANOVA followed by Bonferroni's test.
Data are presented as mean ± s.e.m. or box-and-whisker plots. See also Figure S2 and S4.

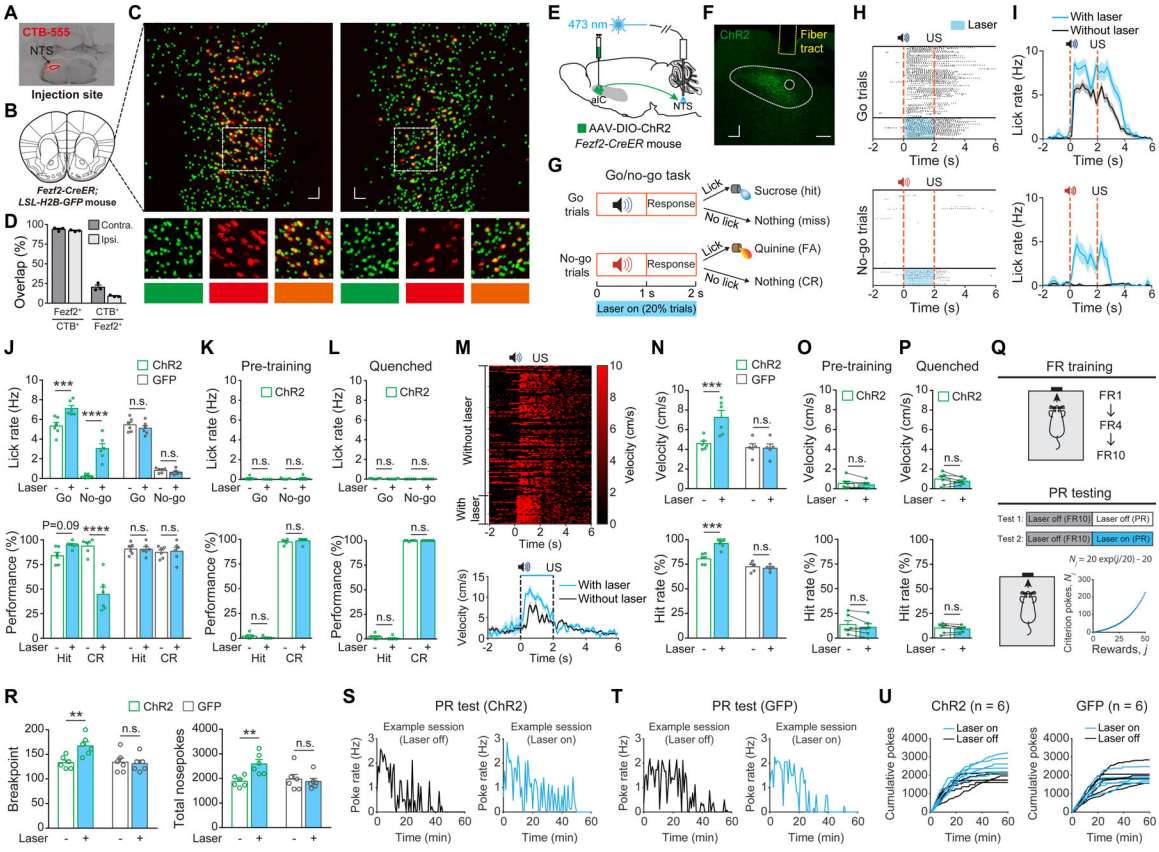

Figure 3. aIC^{Fezf2}→NTS activation promotes motivational vigor and effort

(A) An image showing CTB-555 injection in the NTS in a *Fezf2-CreER;LSL-H2B-GFP* mouse.

(B) A schematic of the brain section containing the aIC.

(C) Top, confocal images of retrogradely labelled aIC^{NTS} neurons (red) and Fezf2^{+} neurons (green) in the contralateral (left) and ipsilateral (right) aIC relative to the injection site in the NTS. Bottom, images of the boxed areas in the top panel. White arrowheads indicate double labelled neurons (yellow). D, dorsal; M, medial.

(D) Left two bars, percentages of co-labelled neurons (yellow) in all the retrogradely labelled neurons (red) in the contralateral (93.91 ± 1.37 %) and ipsilateral (92.08 ± 0.63 %) aIC (n = 3 mice). Right two bars, percentages of CTB^{+} neurons (red) in the Fezf2^{+} neurons (green) in the contralateral (20.36 ± 2.72 %) and ipsilateral (9.01 ± 0.68 %) aIC (n = 3 mice).

(E) A schematic of the approach.

(F) A confocal image showing optic fiber placement and axon fibers in the NTS, which originated from aIC^{Fezf2} neurons. White arrowhead indicates the solitary tract.

(G) A schematic of the experimental design.

(H, I) Licking rasters (H) and average licking rates (I) of a ChR2 mouse in one session. Top, go trials; bottom, no-go trials. Blue rectangles indicate the window of laser stimulation.

(J) Top, lick rate during anticipation period (0–2 s) (ChR2: n = 6 mice, $F_{(1,10)}$ = 86.58, P < 0.0001; go trials, ***P = 0.001; no-go trials, ****P < 0.0001; GFP: n = 6 mice, $F_{(1,10)}$ = 0.59, P = 0.46; go trials, P = 0.061; no-go trials, P = 0.37). Bottom, performance (ChR2:

$F_{(1,10)}$ = 76.68, P < 0.0001; hit, P = 0.091; CR, ****P < 0.0001; GFP: $F_{(1,10)}$ = 0.11, P = 0.75; hit, P > 0.99; CR, P > 0.99). Two-way ANOVA followed by Bonferroni's test.

(K) Behavior of the ChR2 mice (n = 5) at the pre-training stage. Top, licking rates during anticipation period (0–2 s) ($F_{(1,8)}$ = 1.03, P = 0.34; go trials, P = 0.63; no-go trials, P > 0.99). Bottom, performance ($F_{(1,8)}$ = 1.77, P = 0.22; hit, P = 0.59; CR, P = 0.93). Two-way ANOVA followed by Bonferroni's test.

(L) Behavior of quenched ChR2 mice (n = 6) at the late training stage. Top, licking rates during anticipation period (0–2 s) ($F_{(1,10)}$ = 0.40, P = 0.54; go trials, P = 0.50; no-go trials, P > 0.99). Bottom, performance ($F_{(1,10)}$ = 1.26, P = 0.29; hit, P = 0.40; CR, P > 0.99). Two-way ANOVA followed by Bonferroni's test.

(M) Running behavior of a ChR2 mouse in one session. Top, trial-by-trial velocity heatmap. Bottom, average running velocity; blue bar indicates the window of laser stimulation.

(N) Top, running velocity during anticipation period (0–2 s) ($F_{(1,9)}$ = 21.47, P = 0.0012; ChR2, n = 6, ***P = 0.0002; GFP, n = 5, P > 0.99). Bottom, hit rate ($F_{(1,9)}$ = 18.91, P = 0.0019; ChR2, ***P = 0.0005; GFP, P > 0.99). Two-way ANOVA followed by Bonferroni's test.

(O) Behavior of the ChR2 mice (n = 6) at the pre-training stage. Top, running velocity during anticipation period (0–2 s) ($t_{(5)}$ = 1.50, P = 0.19, paired t-test). Bottom, hit rate ($t_{(5)}$ = 1.92, P = 0.11, paired t-test).

(P) Behavior of quenched ChR2 mice (n = 6) after training. Top, running velocity during anticipation period (0–2 s) ($t_{(5)}$ = 1.18, P = 0.29, paired t-test). Bottom, hit rate ($t_{(5)}$ = 1.23, P = 0.27, paired t-test).

(Q) Schematics of the task design for fixed-ratio (FR) and progressive-ratio (PR).

(R) Left, breakpoint: $F_{(1,10)}$ = 11.07, P = 0.0077; ChR2, n = 6, **P = 0.0029; GFP, n = 6, n.s., P > 0.99. Right, total nosepokes: $F_{(1,10)}$ = 16.17, P = 0.0024; ChR2, **P = 0.0011; GFP, n.s., P > 0.99. Two-way ANOVA followed by Bonferroni's test.

(S, T) Nosepoke rate during PR test for a ChR2 (S) and GFP (T) mouse.

(U) Cumulative nosepokes for the ChR2 (left) and GFP (right) mice during PR test.

Data are presented as mean ± s.e.m. See also Figure S4.

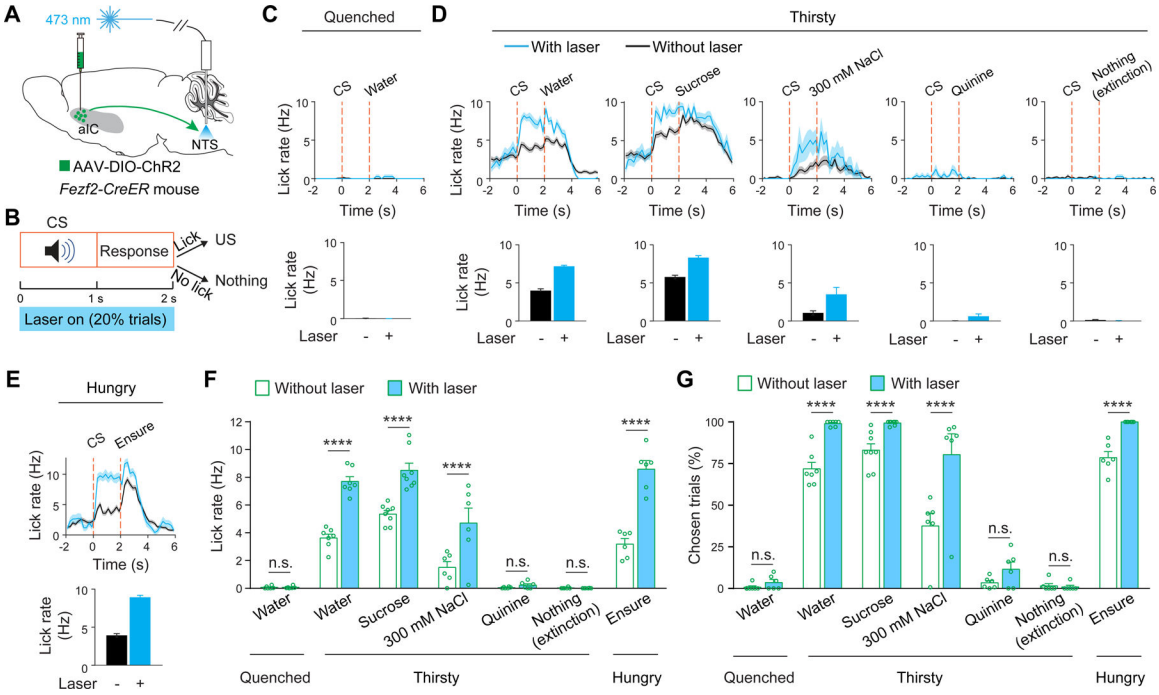

Figure 4. aIC^{Fezf2}→NTS function depends on the perceived values

(A, B) Schematics of the approach (A) and experimental design (B).

(C-E) Average licking rate traces (top) and licking rate during anticipation period (bottom) in representative sessions of differing conditions. (C) Quenched condition. (D) Thirsty condition. (E) Hungry condition.

(F) Licking rate during anticipation period in the ChR2 mice under differing conditions ($F_{(6,38)}$ = 23.96, P < 0.0001; quenched: water, n.s., P > 0.99; thirsty: water, sucrose and NaCl, ****P < 0.0001; thirsty: quinine and extinction, n.s., P > 0.99; hungry: ensure, ****P < 0.0001; two-way ANOVA followed by Bonferroni's test).

(G) Performance, quantified as the fraction of trials the mice licked during the anticipation period, in the ChR2 mice under differing conditions ($F_{(6,38)}$ = 16.45, P < 0.0001; quenched: water, n.s., P > 0.99; thirsty: water, sucrose and NaCl, ****P < 0.0001; thirsty: quinine, n.s., P = 0.24; extinction, n.s., P > 0.99; hungry: ensure, ****P < 0.0001; two-way ANOVA followed by Bonferroni's test).

Data are presented as mean ± s.e.m.

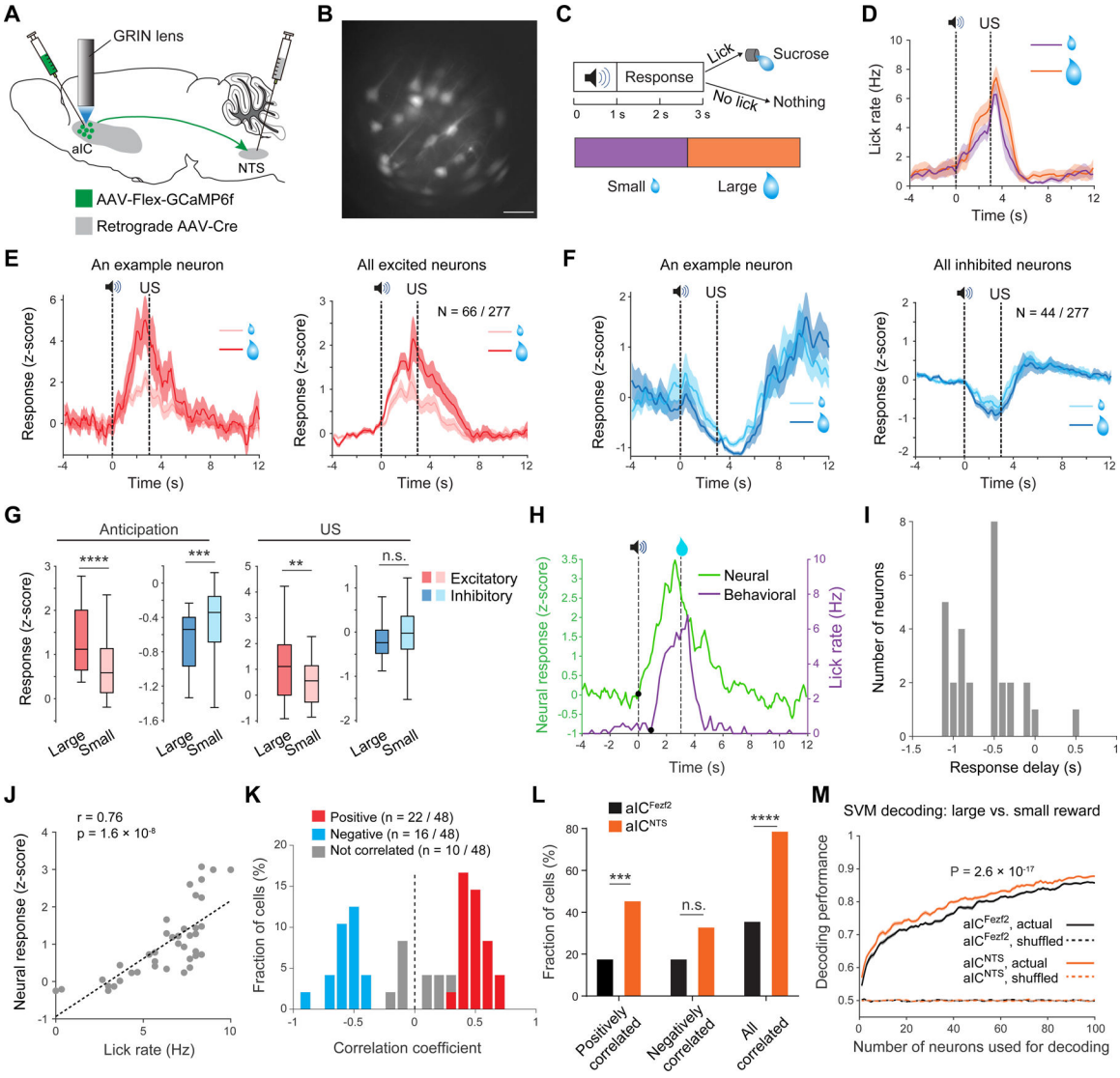

Figure 5. aIC^{NTS} neurons are enriched with the anticipatory vigor signals

(A) A schematic of the approach.

(B) A field of view showing the raw GCaMP6f fluorescence signals in aIC^{NTS} neurons.

(C) A schematic of the task design.

(D) Average licking rates in the small-reward and large-reward blocks.

(E) Activity traces of aIC^{NTS} neurons showing excitatory responses to US. Left, an example neuron; right, all neurons.

(F) Same as E, except that data are from aIC^{NTS} neurons with inhibitory responses.

(G) Quantification of the average responses shown in (E, F), during the anticipation (0–3 s; left) and US (3–5 s; right) periods (**P < 0.01; ***P < 0.001; ****P < 0.0001; n.s., P > 0.05; Wilcoxon signed-rank test).

(H) The timing of CS-induced excitation and licking in an aIC^{NTS} neuron and the corresponding mouse, respectively. Black dots represent change points.

(I) The difference between neural and behavioral change-points for all the CS-excited neurons.

(J) A neuron showing a positive correlation between its responses and licking rates in the 3-s time window immediately after CS onset (Pearson's r = 0.76, P < 0.0001). Each dot represents one trial.

(K) Distribution of all the CS-responsive neurons' Pearson's correlation coefficients calculated as in (J). Red, blue and gray bars represent neurons showing significant positive (P < 0.05), significant negative (P < 0.05) and nonsignificant (P > 0.05) correlations, respectively.

(L) The fraction of aIC^{Fezf2} and aIC^{NTS} neurons showing the significant correlations (positive, ***P = 0.00065; negative, n.s., P = 0.059; all, ****P < 0.0001; χ^2 test).

(M) The performance of aIC^{Fezf2} and aIC^{NTS} neural activities during CS period in decoding large-versus small-reward trials (****P < 0.0001, Wilcoxon signed-rank test). Actual or shuffle: decoding analysis using actual neuron activities in large- and small-reward trials, or neuron activities shuffled across trial types.

Data are presented as mean ± s.e.m. or box-and-whisker plots. See also Figure S5.

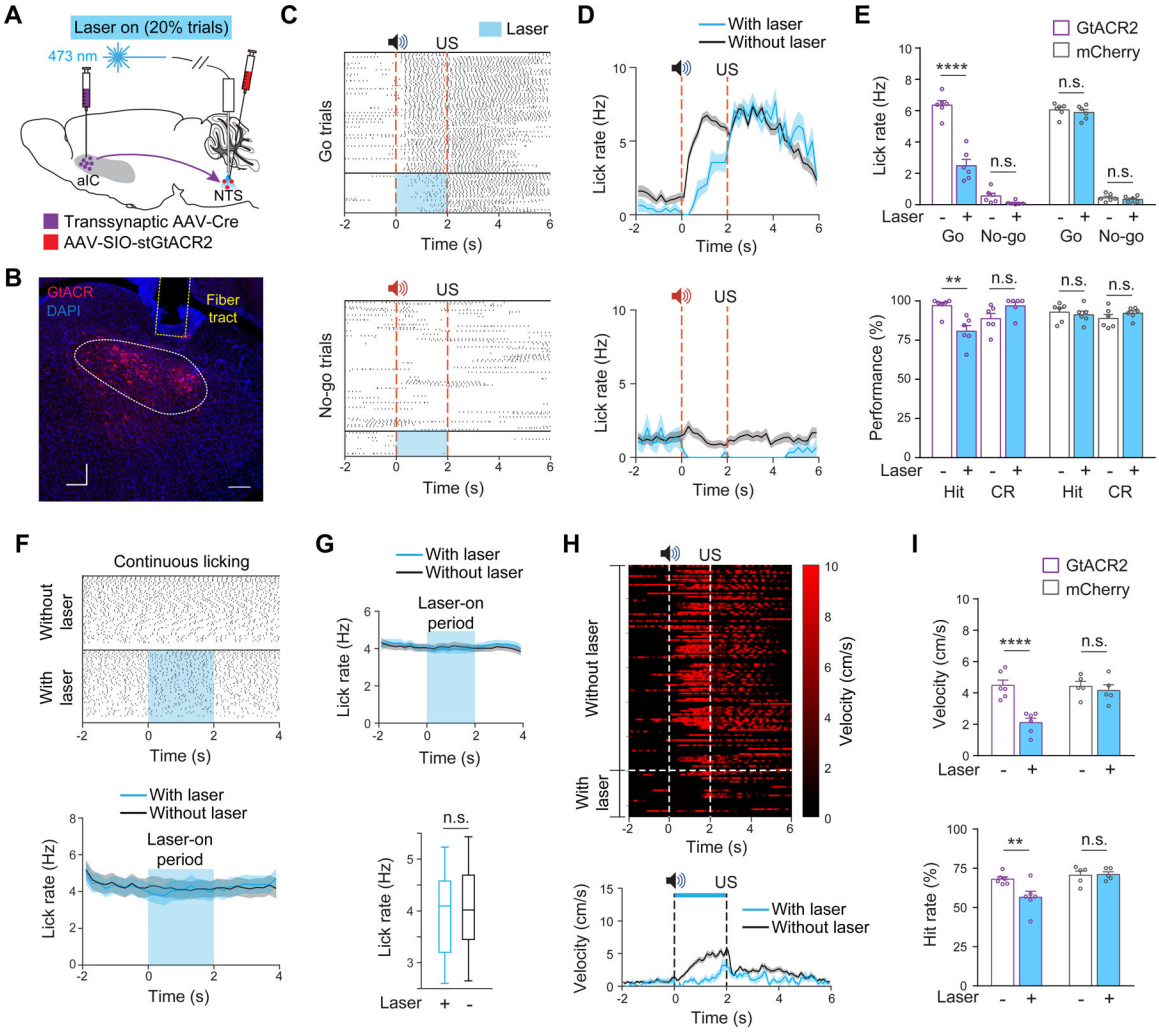

Figure 6. Inhibiting NTS^{Recipient} neurons during anticipation impairs motivational actions

(A) A schematic of the approach.

(B) A confocal image showing the expression of GtACR2 in NTS^{Recipient} neurons and the placement of optical fiber.

(C, D) Licking rasters (C) and average licking rates (D) of a GtACR2 mouse in one session. Top, go trials; bottom, no-go trials. Blue rectangles indicate the window of laser stimulation.

(E) Top, lick rate during anticipation period (0–2 s) (GtACR: n = 6 mice, $F_{(1,10)} = 56.55$, P < 0.0001; go trials, ****P < 0.0001; no-go trials, n.s., P = 0.38; mCherry: n = 6 mice, $F_{(1,10)} = 0.15$, P = 0.71; go trials, n.s., P = 0.27; no-go trials, n.s., P = 0.62). Bottom, performance (GtACR: $F_{(1,10)} = 16.11$, P = 0.0025; hit, **P = 0.0073; CR, n.s., P = 0.17; mCherry: $F_{(1,10)} = 3.74$, P = 0.082; hit, n.s., P = 0.79; CR, n.s., P = 0.19). Two-way ANOVA followed by Bonferroni's test.

(F) Licking behavior of a GtACR2 mouse in the continuous licking task. Top, licking rasters; bottom, average licking rates.

(G) Top, average licking rate across mice; bottom, average licking rate during the 0–2 s window (n = 6 mice; P = 0.30, Wilcoxon signed-rank test).

(H) Running behavior of a GtACR2 mouse in one session. Top, trial-by-trial velocity heatmap; bottom, average running velocity; blue bar indicates the window of laser stimulation.

(I) Top, running velocity during anticipation period (0–2 s) ($F_{(1,9)}$ = 22.69, P = 0.001; GtACR2, n = 6, ****P < 0.0001; mCherry, n = 5, n.s., P = 0.86). Bottom, hit rate ($F_{(1,9)}$ = 12.12, P = 0.0069; GtACR2, **P = 0.0016; mCherry, n.s., P > 0.99). Two-way ANOVA followed by Bonferroni's test.

Data are presented as mean ± s.e.m. or box-and-whisker plots. See also Figure S4.

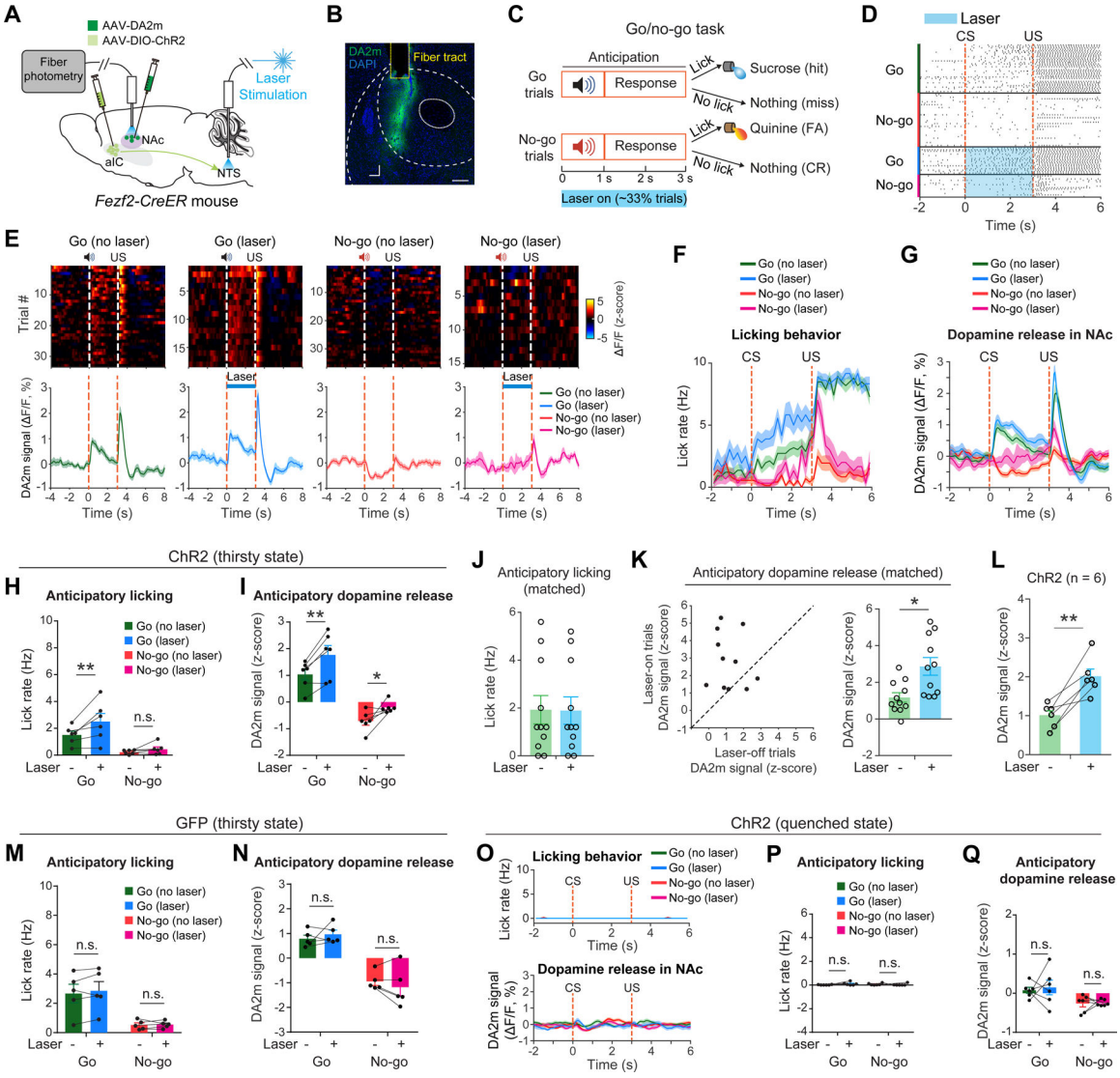

Figure 7. aIC^{Fezf2}→NTS activity promotes NAc dopamine release in a need-dependent manner

(A) A schematic of the approach.

(B) A confocal image showing the expression of DA2m in NAc core and the placement of optical fiber for photometry. Aca, anterior commissure.

(C) A schematic of task structure.

(D-N) Results obtained in thirsty state.

(D) Licking rasters of a ChR2 mouse in one session. Blue rectangles indicate the window of laser stimulation.

(E) Trial-by-trial (top) and average (bottom) dopaminergic activity in the NAc from the same session as that in (D). Blue bars indicate the window of laser stimulation.

(F, G) Average licking rates (F) and DA2m signals in the NAc (G) from the same mouse as in (D).

(H) Licking rate of all ChR2 mice during anticipation period (0–3 s) in different trial types ($F_{(1,10)}$ = 9.645, P = 0.011; go trials, **P = 0.0096; no-go trials, n.s., P = 0.70). Two-way ANOVA followed by Bonferroni's test.

(I) DA2m signals in the NAc of all the ChR2 mice during anticipation period (0–3 s) in different trial types ($F_{(1,10)}$ = 25.94, P = 0.0005; go trials, **P = 0.0034; no-go trials, *P = 0.028). Two-way ANOVA followed by Bonferroni's test.

(J) Licking rate data from a ChR2 mouse in selected go-trials in one session, in which the mouse showed comparable licking rates in each pair of "laser-on" and "laser-off" trials during the anticipation period (0–3 s).

(K) Left, a scatter plot of DA2m signals in pairs of laser-on and laser-off trials where the mouse had comparable anticipatory licking rates. Each dot represents such a pair. Right, quantification of the DA2m signals (*P = 0.019; Wilcoxon signed-rank test).

(L) DA2m signals in the NAc in all the ChR2 mice (n = 6) during anticipation period in the go-trials selected as those in (J, K) ($t_{(5)}$ = 6.80, **P = 0.001, paired t-test).

(M, N) Licking rate (M) and DA2m signals in the NAc (N) of all the GFP mice during anticipation period (0–3 s) in different trial types. (M) $F_{(1,8)}$ = 0.73, P = 0.42; go trials, P = 0.41; no-go trials, P > 0.99. (N) $F_{(1,8)}$ = 2.02, P = 0.19; go trials, P = 0.81; no-go trials, P = 0.58. Two-way ANOVA followed by Bonferroni's test.

(O-Q) Results were obtained from the same mice as in (D-L), but in quenched state.

(O) Example plots showing the absence of CS-evoked licking (top) and DA2m signals in the NAc (bottom) from the same mouse as that in (D-G).

(P) Same as (H), except that data are from quenched state ($F_{(1,10)}$ = 0.69, P = 0.43; go trials, n.s., P = 0.20; no-go trials, n.s., P = 0.81). Two-way ANOVA followed by Bonferroni's test.

(Q) Same as (I), except that data are from quenched state ($F_{(1,10)}$ = 0.11, P = 0.74; go trials, n.s., P = 0.91; no-go trials, n.s., P = 0.99). Two-way ANOVA followed by Bonferroni's test. Data are presented as mean ± s.e.m. See also Figure S6.

KEY RESOURCES TABLE

REAGENT or RESOURCE	SOURCE	IDENTIFIER
Antibodies		
Chicken polyclonal anti-GFP	Aves Labs	Cat# GFP1020; RRID:AB_10000240
Rabbit polyclonal anti-RFP	Rockland	Cat# 600-401-379; RRID:AB_2209751
Rabbit polyclonal anti-tyrosine hydroxylase	Millipore	Cat# AB152; RRID:AB_390204
Bacterial and virus strains		
AAV5-Ef1a-DIO-hChR2(H134R)-eYFP	UNC Vector Core	N/A
AAV9-CAG-Flex-GFP	UNC Vector Core	N/A
AAV1-Syn-Flex-GCaMP6f-WPRE-SV40	Chen et al., 2013	Addgene 100833
AAV1-hSyn-SIO-stGtACR2-FusionRed	Mahn et al., 2018	Addgene 105677
AAV-Ef1a-mCherry-IRES-Cre (retrograde)	Fenno et al., 2014	Addgene 55632
AAV1-hSyn-Cre-WPRE-hGh	Penn Vector Core	N/A
AAV9-hSyn-DA2m	Vigene Biosciences	N/A
AAV2/9-CAG-Flex-mKate-T2A-TVA	HHMI Janelia Research Campus	N/A
AAV2/9-CAG-Flex-mKate-T2A-N2c-G	HHMI Janelia Research Campus	N/A
Rbv-CVS-N2c-ΔG-GFP	HHMI Janelia Research Campus	Addgene 73461
Experimental models: Organisms/strains		
Mouse: Fezf2-2A-CreER	Matho et al., 2021	JAX stock# 036296
Mouse: Rosa26-loxp-STOP-loxpH2B-GFP	He et al., 2012	N/A
Software and algorithms		
ImageJ (Fiji) software	NIH	https://fiji.sc/
MATLAB	Mathworks	https://www.mathworks.com/products/matlab.html
GraphPad Prism 7	GraphPad Software	https://www.graphpad.com/
Original code	This paper	https://figshare.com/articles/software/Codes_for_insular-NTS_paper/16915519